Engineering Geology 369 (2026) 108818



Contents lists available at ScienceDirect

Engineering Geology

journal homepage: www.elsevier.com/locate/enggeo

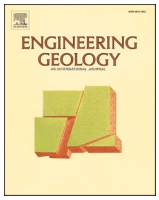

Integrated GBInSAR and thermo-mechanical modeling for rock slope displacement analysis across geometrical complexities

Luca Cifeca Recinella [a,*], Giuseppe Dattola [a], Carlo Rivolta [b], Davide Leva [b], Giovanni Battista Crosta [a]

[a] Dept. Of Earth and Environmental Sciences, Università degli Studi di Milano Bicocca, Milan, MI, Italy
[b] Ellegi Srl, Rovello Porro, CO, Italy

ARTICLE INFO

Keywords:
Rock wall monitoring
Elasto-thermal modeling
Temperature effects
GBInSAR
LOS Displacement

ABSTRACT

Repeated thermal cycles influence rock slope evolution inducing stresses that can initiate and propagate fractures. Ground-Based Interferometric Synthetic Aperture Radar (GBInSAR) monitors the mechanical behavior and superficial displacement, including thermally-induced, useful for precursor displacements detection before landslide onset and collapse. A coupled thermo-mechanical Finite Element Method (FEM) is used to investigate thermal effects on rock slope deformations to (i) understand how slope geometry influences heat flux and stress, (ii) assess thermo-mechanical parameter impact on the thermo-mechanical response, and (iii) simulate slope geometry and aspect effects on system response through different boundary temperature. Finally, simulated FEM superficial displacement maps are compared with GBInSAR measurements from two Italian Alps sites. Results demonstrate that curvature and changes in slope inclination significantly concentrate temperature increments and associated stresses. Specific heat affects both temperature distribution and displacements, while Young's modulus and thermal expansion coefficients influence displacement and stress magnitudes. External temperatures controlled by slope aspect impact movement modes, producing torsional effects, especially for slender features. The numerical predictions and GBInSAR data comparison reveal a strong agreement in displacement distribution, validating the model ability to capture observed deformation patterns. These findings highlight the role of thermal forcing in rock slope deformation and its sensitivity to geometric features and material properties. The results offer valuable insights for monitoring planning, by identifying thermally sensitive areas, for interpreting field data, isolating thermal contributions from total displacements; and for slope stability analysis, by providing a framework to assess thermo-mechanically induced stress and deformation under current and future climatic conditions.

1. Introduction

Rock cliffs are characterized by sub-vertical walls of varying orientations, with the rock mass more or less intensely subdivided into blocks and pillars. These geological features are susceptible to large temperature fluctuations and slope instability, which can manifest as a transition from slow creeping to catastrophic collapse. Such events pose significant hazards, as falling rock masses can impact structures, facilities, and settlements, leading to severe damage and fatalities (Bourrier et al., 2009; Clauge and Stead, 2012; Olmedo et al., 2018; Selby, 1993; Whalley, 1979). In the most recent decades, a series of large pillar and rocky cliffs collapse have been recorded throughout the European Alps, particularly at elevated altitudes where permafrost thawing and degradation have compromised the stability of the cliffs (Bonometti et al., 2025; Noetzli et al., 2007; Noetzli and Gruber, 2009). Consequently, monitoring techniques (e.g., laser scanner, UAV, satellite, interferometry, in-situ instrument) play a crucial role in understanding rock slope instabilities and mitigating associated risks. Ground-Based Interferometric Synthetic Aperture Radar (GBInSAR) stands out as a powerful remote sensing tool, enabling continuous, high-precision monitoring of slope displacements. Operating on radar interferometry principles, GBInSAR detects phase differences between successive radar images to measure displacements along the line-of-sight (LOS), achieving millimetric accuracy even under varying weather and lighting conditions

* Corresponding author.
E-mail addresses: l.cifecarecinella@campus.unimib.it (L. Cifeca Recinella), giuseppe.dattola@unimib.it (G. Dattola), carlo.rivolta@lisalab.com (C. Rivolta), davide.leva@lisalab.com (D. Leva), giovannibattista.crosta@unimib.it (G.B. Crosta).

https://doi.org/10.1016/j.enggeo.2026.108818
Received 15 July 2025; Received in revised form 23 March 2026; Accepted 12 May 2026
Available online 14 May 2026
0013-7952/© 2026 The Authors. Published by Elsevier B.V. This is an open access article under the CC BY license (http://creativecommons.org/licenses/by/4.0/).

(Leva et al., 2003; Woods et al., 2021). Its widespread application in landslide monitoring is attributed to its capability to provide both high spatial and temporal resolution data, which are essential for early warning systems and for modeling slope kinematics (Tarchi et al., 2003). Furthermore, its integration with other sensors (e.g., GNSS, extensometers, crack meters and thermal sensors for superficial and deep temperature measurements) significantly enhances the diagnostic and predictive capacity of monitoring networks in areas where steep topography and permafrost create highly temperature-sensitive slopes (Agliardi et al., 2013; Leva et al., 2005). Noticeably, while seasonal displacement trends commonly observed by in-place extensometers can partially reflect the physical thermal expansion of the instruments themselves, GBInSAR acquires remote LOS measurements from a sensor located away from the slope. Any thermally induced deformation of the radar unit is expected to manifest mainly as a quasi-rigid, common-mode offset over the whole scene, which can be largely mitigated by referencing the displacement field to a stable area and by spatial filtering. For this reason, GBInSAR time series are generally less prone to spurious instrument-related seasonal signals. When combined with conventional in-place sensors, they provide a complementary view that is uniquely useful for interpreting displacement mechanisms in thermally sensitive rock slopes.

Several triggering factors generate rockfalls, including earthquakes, intense rainfall, permafrost degradation, and temperature fluctuations, which are often governed by a complex interplay of structural, lithological, and climatic conditions (Bonometti et al., 2025; Crosta and Agliardi, 2003; Frattini et al., 2008; Krautblatter et al., 2013; Palladino et al., 2018; Valagussa et al., 2014). Among these mechanisms, diurnal and seasonal temperature variations are particularly influential. Repeated cycles of thermal expansion and contraction generate internal stresses that eventually lead to the initiation and propagation of fractures. For example, Collins and Stock (2016) and Collins et al. (2018, 2019) documented thermal fracture openings in granite exfoliation sheets ranging from 12.7 mm to 44 mm during warm days with significant temperature swings $7^{\circ}C$ to $39^{\circ}C$ has been documented (Collins and Stock, 2016; Collins et al., 2018, 2019). Merrien-Soukatchoff and Gasc-Barbier (2023) concluded that thermally induced deformation is strongly influenced by topography and aspect. At Les Rochers de Valabres (France), Gunzburger and Merrien-Soukatchoff (2011) reported daily temperature amplitudes up to 21°C, highlighting the influence of solar exposure. Mufundirwa et al. (2011) observed fracture openings of up to 0.21 *mm* associated with temperature variations between $-4^{\circ}C$ and $23^{\circ}C$. However, most of these studies were limited to local or single fracture variations rather than large-scale slope responses.

To scale these observations, numerical modeling serves as an effective tool for reproducing onset phenomena and assessing the mechanical behavior of rock cliffs prior to failure (Crosta et al., 2003; Frankovská et al., 2015; Sarkar et al., 2012; Wang et al., 2017; Yang et al., 2015). Numerous studies have demonstrated the effectiveness of thermo-mechanical simulations, particularly using the Finite Element Method (FEM) and distinct element codes. For instance, Marmoni et al. (2020) and Mamot et al. (2021) showed that discontinuities strongly influence heat propagation and the localization of plastic strain, with the upper 5–7 m of the rock mass exhibiting the greatest sensitivity to thermal fatigue. Similarly, FEM simulations by Villarraga et al. (2021) indicated that thermal fluctuations induce significant stress concentrations at fracture tips, driving propagation without other external triggers. Greif et al. (2017) investigated the thermally driven deformation of a natural rock arch using a 3D FEM model, revealing that progressive structural weakening increases susceptibility to failure over time due to thermal fatigue. In a tropical context, Do Amaral Vargas et al. (2013) explored via FEM models how steeply dipping fractures with low cohesion are easily destabilized under large diurnal temperature ranges.

Despite these advancements, the aforementioned modeling studies primarily focused on relatively small, metric-scale slope portions. An exception is the work of Noetzli et al. (2007) and Noetzli and Gruber (2009), who investigated the large-scale thermal regime of Alpine permafrost using 3D transient heat transfer models on realistic topographies. However, their modeling focuses exclusively on the thermal domain, without explicitly addressing the mechanical response. Conversely, Gischig et al. (2011) showed, using two-dimensional conceptual models of the Randa landslide, that thermo-elastic stresses can propagate to depths exceeding 100 m, promoting incremental shear displacements and contributing to long-term instability.

From an engineering geology perspective, interpreting the thermo-mechanical behavior of rock slopes is fundamental for hazard assessment and early warning system design. A major challenge arises from monitoring tools like GBInSAR, which capture complex displacement fields coupling reversible thermo-elastic strains with irreversible damage. Consequently, the primary aim of this work is to disentangle these signals by coupling long-term GBInSAR surface displacement data with Finite Element Method (FEM) modeling. We investigate temperature changes and induced displacements across simplified geometries (e.g., cubic elements, convex faces, and isolated pillars) and two real rock cliff topographies, considering variable conditions from intact rock to heavily fractured masses. By constructing these theoretical temperature-controlled displacement maps, we establish a mandatory baseline that allows engineering geologists to: (i) identify topographic sectors most susceptible to thermal fatigue to prioritize monitoring efforts; and (ii) effectively filter reversible thermal noise from radar images, isolating genuine precursors to failure.

2. Case study

2.1. Geological setting

2.1.1. Scaiùn cliff

Val Masino is a tributary valley of the Valtellina Valley in Northern Italy (Fig. 1a), characterized by a rugged mountainous landscape. It features a significant altitudinal change, from 580 m a.s.l. (Ponte del Baffo) to 3678 m a.s.l. (Monte Disgrazia). The morphology reflects a glacially shaped valley system framed by steep slopes and ridges. Geologically, the area lies north of the Tonale Tectonic Line and is predominantly composed of intrusive rocks from the Tertiary Val Masino Pluton. Metamorphic rocks of the Margna Crystalline Complex and the Languard-Tonale system also occur locally, consisting of mica schists, gneisses, quartzites, and amphibolite with variable foliation. Beyond the Tonale Line, the structural framework is governed by the Val d'Agua Line, and the Cataeggio Fault, which influence lithological boundaries and dip directions, generally trending north. Quaternary surface deposits are varied, including Holocene and Late Glacial moraines, talus deposits, alluvial fans, terraces, and peat-rich sediments in glacial over deepened basins. The slopes in the area have a history of widespread instabilities, mostly large block rockfalls and rockslides. Notable examples include three events at Sasso Bisolo Mt-Pezza in 1931, 1977, and 1991, influenced by local quarrying and controlled by the Serizzo foliation (Crosta, 1992). Another event occurred nearby at Ponte del Baffo in 1961. Among the most critical slopes is the Scaiùn cliff, above the village of Cataeggio (Fig. 1) at the southeastern margin of the Masino–Bregaglia pluton. The rock face comprises tonalite and granodiorite (locally known as serizzo), with extensive debris cones and boulder fields at its base, indicative of intense rockfall activity that has left decametric blocks embedded within the village. The main joint sets structuring the rock mass are K1 (163/59°), which is parallel to the foliation plane and K2 (165/86°). Additional joint families are K3 (69/86°), K4 (94/53°), and K5 (263/81°) that contribute to lateral release mechanisms, forming isolated rock prisms prone to planar sliding. These structural conditions were confirmed by photogrammetric and radar data following the February 4, 2019, collapse, which involved more than 7900 m^3 of rock and highlighted the importance of persistent discontinuities and foliation-parallel failure surfaces (Dei Cas et al., 2021). The

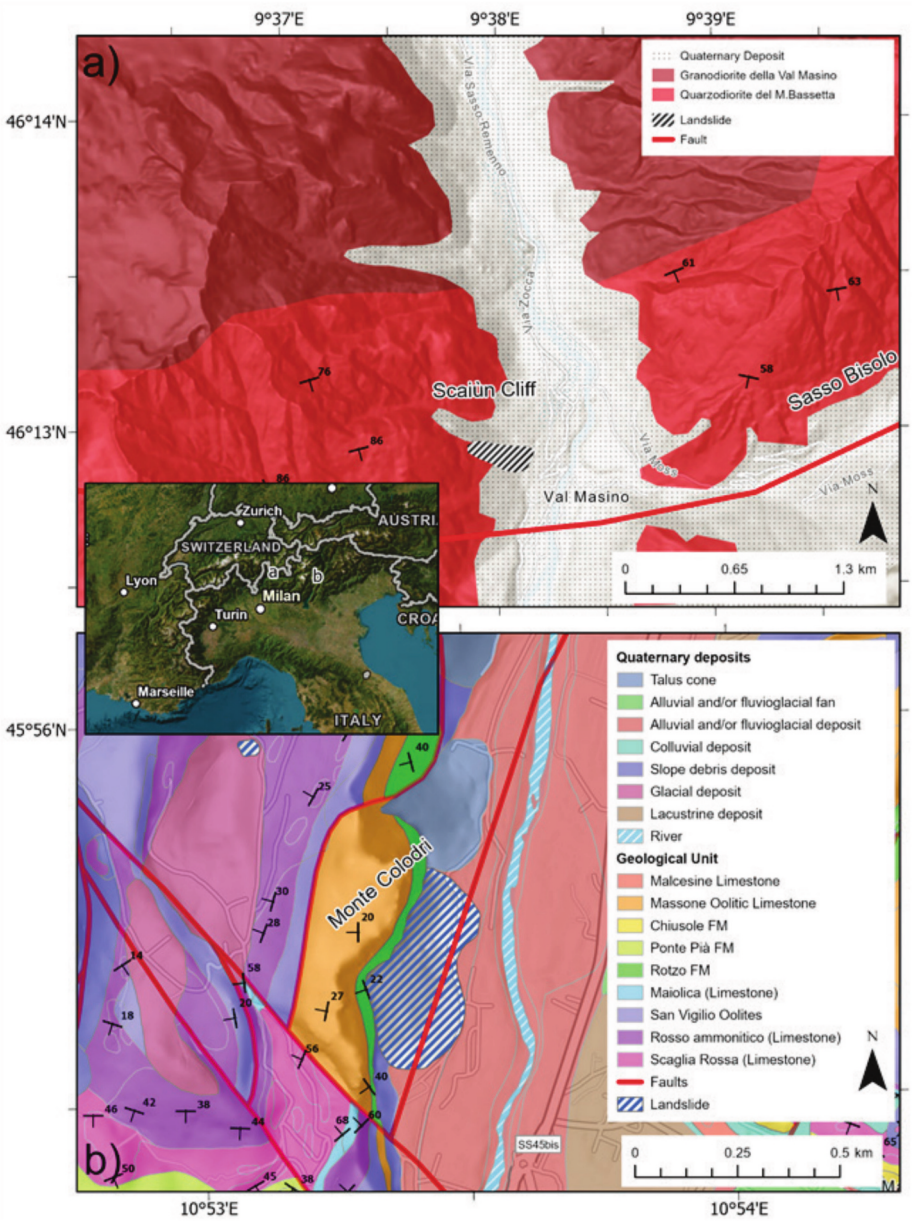

Fig. 1. Location and geological maps of the two study areas in the Italian Alps: (a) Scaiùn cliff, Val Masino-Cataeggio (SO); (b) Monte Colodri, Arco di Trento- (TN).

serizzo has a thermal expansion coefficient of 0.0061 $mm/m^{\circ}C$. The study area features an alpine climate with cold winters and mild summers. The mean annual temperature is approximately 6 °C, with annual average daytime and nighttime temperatures of 10 °C and 1 °C. Seasonally, average summer temperatures range from 20 °C (diurnal) to 11 °C (nocturnal), while winter months experience average highs of −1 °C and lows of −9 °C. Average annual precipitation is 1977 mm—distributed as 82% rain and 18% snow or hail—with a maximum in June and a minimum in January.

2.1.2. *Monte colodri*

Arco is located in the southern part of Trentino (Autonomous Province of Trento), within the Sarca river valley, north of Lake Garda (Fig. 1c). It lies at an altitude of approximately 90 m a.s.l. and is surrounded by prominent carbonate reliefs. These features include Monte Brento (1545 m) and Monte Casale (1632 m) to the north; Monte Stivo (2059 m), Monte Velo, and Monte Creino to the northeast; and Monte Biaìna (1413 m), Monte Baone, and Monte Colodri to the west. Monte Colodri is situated in close proximity to the built-up area and is popular among tourists and climbers.

The area is part of the Southern Alps, specifically within the Trentino Platform (CARG sheet 080 'Riva del Garda', ISPRA). It corresponds to a significant structural bundle predominantly trending NNE-SSW, delimited to the west by the Ballino Line and to the east by the Adige Valley Line. Monte Colodri itself is situated between the Rudere di San Martino fault and the northern branch of the eastern Val Lomasone fault (LOE). These tectonic structures define uplifted structural prisms, bounded by high-angle reverse faults and occasionally associated with transpressional structures, primarily formed during the Valsuganese phase (Upper Miocene). Monte Colodri largely consists of Mesozoic carbonate deposits, predominantly Dolomia Principale (Upper Carnic-Noric) and Grey Limestone (Lower Lias) (Castellarin et al., 2005).

The Dolomia Principale outcrops manifest as substantial, stratified, light grey banks, characterized by pronounced fracturing and localized effects from secondary faults. These outcrops frequently coincide with surface and deep karst phenomena. These characteristics render Monte Colodri susceptible to instability. The main joint sets structuring the rock mass are K1 (65/66°), K2 (18/82°) and K3 (298/83°) The

occurrence of rockfall events, localized detachments, and toppling has been well-documented on the IdroGEO platform. *(https://idrogeo.isprambiente.it)*.

Influenced by nearby Lake Garda, the local alpine climate features relatively mild conditions with a mean annual temperature of 8 °C (averaging 13 °C during the day and 4 °C at night). Summers are hot, with July temperatures averaging 23 °C (diurnal) and 14 °C (nocturnal). In contrast, winters are cold, with January averages dropping to 2 °C (day) and − 6 °C (night). The area receives an average of 1923 mm of annual precipitation, reaching a maximum of 222.5 mm in November, which falls primarily as rain (85%), alongside snow and hail (15%).

2.2. GBInSAR monitoring

2.2.1. Scaiùn cliff

A permanent GBInSAR system (LiSALab, operated by Ellegi Srl) was installed on the western side of the valley, at an approximate altitude of 800*m* a.s.l. This unit monitors the east-facing Scaiùn slope across the valley, with an oblique and upward-looking line-of-sight (LOS) extending to elevations of more than 1500*m a.s.l.*. For this system, negative LOS displacement values indicate movement towards the sensor (i.e. downslope displacements), while positive LOS displacement values indicate movement away from the sensor (i.e. upslope displacement). In 2024, the monitoring system collected over 300 radar images, processed with 24-h averaging to minimize atmospheric and thermal noise. The displacement data exhibited a discernible seasonal trend, with substantial deformation observed in the central sector of the slope. This area experienced average annual displacements of −9 mm, with maximum cumulative values reaching −31 mm. These observations are consistent with previous years (−9 mm in 2023, −11 mm in 2022) and suggest that the slope dynamics (at this stage) is primarily governed by thermo-mechanical effects. During summer, the radar detected small positive displacements, interpreted as thermal expansion of the rock mass, potentially due to joint opening and minor outward bulging. Conversely, autumn and early winter exhibited pronounced negative displacements, reaching up to −10 mm/month. These are consistent with thermal contraction, joint closure, and possible ice-wedging effects. Of the 55 Points Of Interest (POIs) monitored across the slope, only the central group demonstrated significant motion, with POI#30 reaching −25.1 mm in 2024 (Fig. 2). All other zones, including the southern, northern, and former collapse areas, remained within the radar noise threshold (±0.4 mm), thereby confirming general slope stability. The upward and across-valley LOS geometry is of crucial importance in understanding these detected trends.

2.2.2. Monte colodri

As above said, Monte Colodri cliffs are characterized by prominent geological fractures, including two large rock pillars (total volume of approximately $33,000m^3$). These pillars (with a thickness of ca 15 m) are separated from the primary rock mass by sub-vertical discontinuities, oriented parallel to the slope. To monitor the stability of the slope, a GBInSAR was periodically installed at a stable location to conduct multiple observation campaigns. A 3.5-day monitoring campaign in July 2024 acquired 1030 radar images. This dataset was compared with both an initial reference dataset (acquired in October 2023), and data from a third campaign (April–May 2024). This comparative analysis allows for an assessment of both long-term deformation trends (over 266 days) and medium-term changes (over 80 days). During the most recent monitoring period, the slope evidenced consistent stability, with an average minimal displacement across the cliff face of −0.1 mm and standard deviation of 0.3 mm. This finding aligns with previous observations and indicates no significant short-term movement. However, a more complex picture emerges when comparing the data with the October 2023 baseline. The analysis reveals an initial phase of movement towards the radar during the winter months, followed by a gradual reversal as the rock face slowly shifts away from the radar during spring and summer. This seasonal pattern is hypothesized to be driven by thermal expansion and contraction of the rock masses in response to daily and seasonal temperature fluctuations. Specific areas, designated E, E1, and G, exhibited more pronounced displacements, with peak values of −3.5 mm, −3.0 mm, and + 1.8 mm, respectively (Fig. 3). Despite these peaks, average movements remained below 1 mm. A region previously exhibiting stability, designated as L, demonstrated novel deformation during the fourth campaign, with displacements reaching a maximum of −1.2 mm, suggesting this area merits further observations in subsequent campaigns. A comparison of the results with the third campaign (April–May 2024) reveals a general trend of backward movement (away from the radar), with average displacements ranging from 0.3 mm to

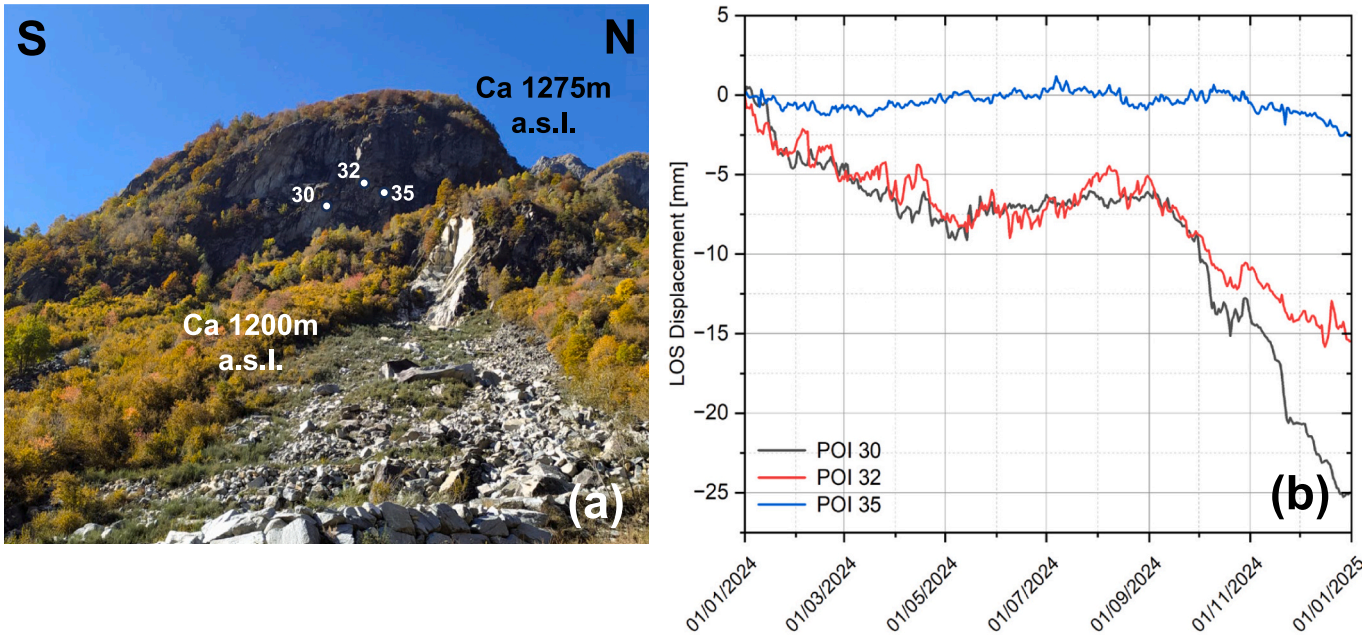

Fig. 2. (a) View of the Scaiùn cliff and monitoring area; (b) Displacement along LOS for POIs #30, #32, #35. The white point indicates the approximate location of the displayed points of observation.

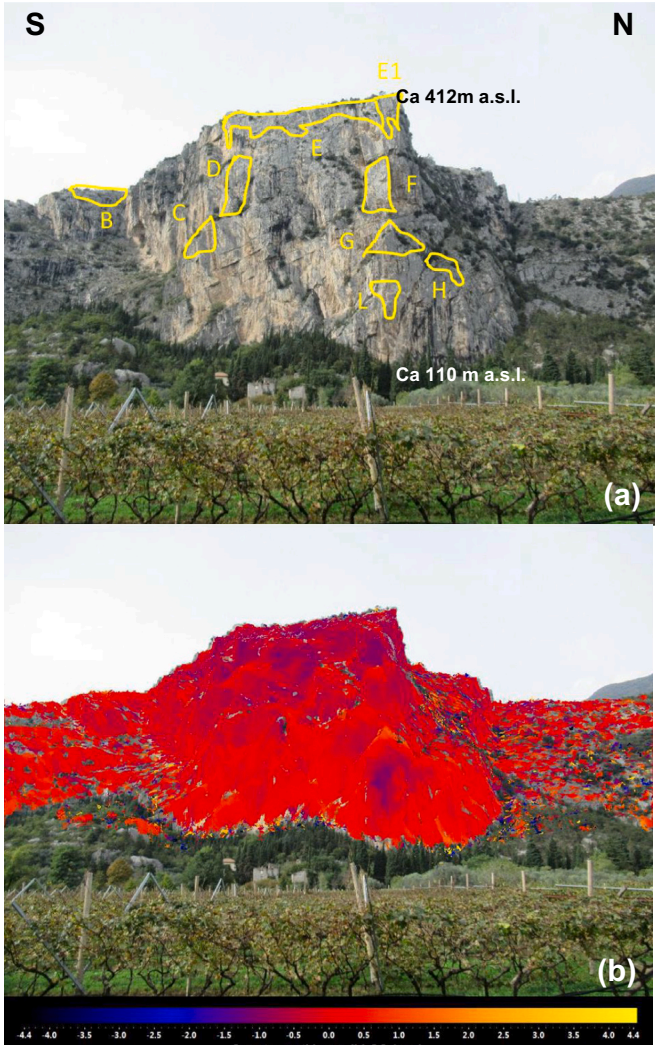

Fig. 3. Monte Colodri from frontal view showing: (a) the identified main moving sectors; (b) LOS displacement map for long-term measurements (269 day, October 2023–July 2024).

1.5 mm depending on the zone, and local peaks reaching 4.1 mm. These variations indicate the differing responses of various portions of the rock face to environmental conditions, particularly where geological discontinuities are more pronounced or where there is greater exposure to sunlight. It is hypothesized that these movements are principally driven by thermal responses rather than imminent structural instability.

3. Numerical simulations

To investigate the thermal effects on rock slope deformational behavior and to support a clear understanding and analysis of monitoring data, a series of numerical models were developed. These models consider both simplified geometries and the two aforementioned case studies. The performed numerical analyses include both steady state thermal-elastic and transient thermal-elastic models.

3.1. Mathematical models

A mathematical thermal model is based on the energy balance equation, expressed in its integral form as:

$$-\int_{\partial\Omega} q\cdot\hat{n}\, dS + \int_{\Omega} r d\Omega = \int_{\Omega} c\rho \frac{\partial T}{\partial t} d\Omega \tag{1}$$

in which c is the specific heat, ρ is the material density, T is the temperature, r is the source or sink of heat, q is the heat flux vector, $\hat{n}$ is the outward normal vector, and Ω is the integration domain while $\partial\Omega$ is its boundary. Furthermore, the heat flux is given by the Fourier's law, given by:

$$q = -\boldsymbol{k}\nabla T \tag{2}$$

being $\boldsymbol{k}$ is the conductivity tensor and ∇ is the nabla operator. Since the material is considered thermally isotropic ($\boldsymbol{k} = k\boldsymbol{I}$), after substituting Eq. (2) into (1) become:

$$\int_{\partial\Omega} (k\nabla T)\cdot\hat{n}\, dS + \int_{\Omega} r d\Omega = \int_{\Omega} c\rho \frac{\partial T}{\partial t} d\Omega \tag{3}$$

Applying the divergence theorem, and since the balance equation must be met for any domain Ω, the above equation becomes:

$$\nabla\cdot(k\nabla T) + r = c\rho \frac{\partial T}{\partial t} \tag{4}$$

which is the classical differential equation of heat flow whose main unknown is the temperature function $T = T(t,x,y,z)$.

To fully define the problem, an initial condition is required, having the form:

$$T(t=0,x,y,z) = T_0(x,y,z) \tag{5}$$

being $T_0(x,y,z)$ the initial spatial temperature distribution. The boundary domain is divided into two parts: one part ($\partial\Omega_N$) where no heat flux is imposed, that is:

$$q\cdot\hat{n} = -k\nabla T\cdot\hat{n} = 0 \tag{6}$$

and ($\partial\Omega_D$) where the temperature is imposed, i.e.:

$$T(t,x,y,z) = T_D(t,x,y,z) \tag{7}$$

where $(x,y,z) \in \partial\Omega_D$ and T_D is the air temperature. As no heat source/sinks are considered in the subsequent simulations, $r = 0$.

According to the continuum mechanics theory, the problem is governed by equilibrium, compatibility and constitutive equations. Equilibrium equation is:

$$\text{div}\,(\boldsymbol{\sigma}) + \rho\boldsymbol{g} = 0 \tag{8}$$

in which $\boldsymbol{\sigma}$ is the stress tensor, $\boldsymbol{g}$ is the gravity acceleration vector, ρ is the material density and div $(\cdot)$ is the tensorial divergence. Compatibility equation links the displacement to the strain field, and in case of small displacements and rotations, this relationship is expressed as:

$$\boldsymbol{\varepsilon} = \frac{1}{2}\left[\nabla\boldsymbol{u} + (\nabla\boldsymbol{u})^t\right] \tag{9}$$

being $\boldsymbol{\varepsilon}$ the strain tensor, $\boldsymbol{u}$ the displacement vector, and apex t stands for the transpose operator.

In the following numerical simulations, the linear isotropic elastic material is chosen, and the constitutive law has the following form:

$$\boldsymbol{\sigma} = \boldsymbol{D}^e[\boldsymbol{\varepsilon} - \alpha(T - T_0)\boldsymbol{I}] \tag{10}$$

being α thermal expansion coefficient and $\boldsymbol{D}^e$ the elastic stiffness tensor which depends on two material parameters: Young's modulus E and Poisson's ratio ν.

For the boundary condition, the domain surface is split up into two parts. In one part the displacements are imposed. Mathematically this condition is expressed as:

$$\boldsymbol{u}(t,x,y,z)\cdot\hat{\boldsymbol{n}}_d = u_0(x,y,z) \tag{11}$$

being u_0 the imposed displacement and $\hat{\boldsymbol{n}}_d$ the direction of locked displacement. In the other part no surface force is applied and therefore

the following relationship is set:

$$\boldsymbol{\sigma}\hat{\boldsymbol{n}} = \mathbf{0} \tag{12}$$

3.2. Simulations with simplified geometry

Thermo-elastic analyses were conducted on simplified geometries to investigate the thermo-mechanical response of a slope system subjected to sinusoidally varying external temperature conditions. The objective of this preliminary work was to gain insights into the thermo-mechanical phenomena involved, providing a basis for extension to more realistic and complex slope geometries.

3.2.1. Pillar geometry

The simplified geometry, a prism with a trapezoidal base, is illustrated in Fig. 4, along with its dimensions. The pillar was discretized in 288 portions using 8 horizontal, 3 vertical and 7 oblique planes. The mesh comprises 134,934 linear tetrahedral elements and 25,948 nodes. The material properties, defined as Set01 in Table 1, are uniform.

For the thermo-elastic analysis, both mechanical and thermal boundary conditions were imposed on each boundary surface. To avoid any rigid movement, displacement constraints were applied along the z-direction on surface (2) (see Fig. 4), along the x-direction on surface 1, and along the y-direction at the intersection of surface (1) and surface (2) (surface are those encircled in Fig. 4). Regarding thermal conditions, convective boundary conditions were applied to all surfaces except surfaces (1) and (2) to simulate the heat exchange between the model surface and the surrounding air. The evolution of this boundary condition is characterized by the following relationship

$$T(t) = T_0 + A\sin\left(\frac{2\pi}{t_p}t + \varphi_0\right) \tag{13}$$

where T_0 is the initial temperature, A is the temperature amplitude, t_p is the period, and φ_0 is the initial angle phase. Hence, the maximum and minimum temperatures are $T_0 + A$ and $T_0 - A$, respectively. This function approximates real meteorological data collected at a weather station. The initial condition for the entire system was a uniform temperature of $0^{\circ}C$. The analysis was structured into three distinct stages: 1) application of the gravitational force to establish in situ stress conditions; 2) clearing of computed displacements to include displacements only due to thermal effects; 3) application of the thermal load, simulating the temperature variations over a period of many years.

The thermo-elastic analysis reveals a thermal front propagating within the system delayed with respect to the external thermal input (Fig. 5). Beyond the first year, where temperatures are affected by the

Table 1
Parameters of material used in numerical analysis.

Parameter	Set 01	Set 02
Young's module $[N/m^2]$	7.50E+10	1.00E+10
Poisson's ratio $[-]$	0.3	0.3
Unit weight $[kN/m^3]$	27.4	25
Thermal Expansion Coefficient $[1/K]$	8.00E-06	5.00E-06
Thermal Conductivity $[J/(m{\cdot}day{\cdot}K)]$	260,000	216,000
Specific Heat $[J/(kg{\cdot}K)]$	900	900

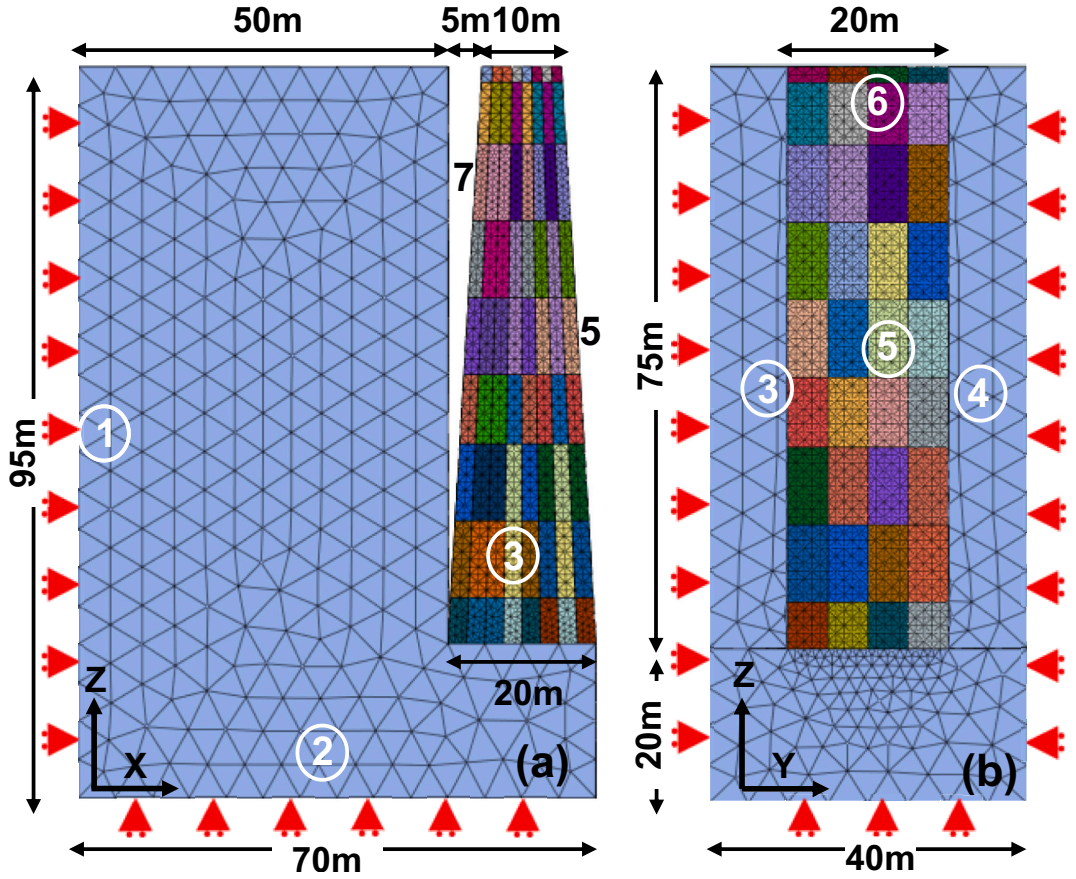

Fig. 4. Simplified pillar shape with a surrounding area (model box) and corresponding mesh used in the analyses: (a) Lateral view; (b) Frontal view. The different colors represent the 288 portions generated from horizontal, vertical, and oblique planes. The minimum mesh size is 1 m and the maximum one is 15 m. Numbers within circles refer to the surface identification. Surfaces (1) and (2) represent the faces of the domain where displacement constraints (red symbol) and no-flux conditions were applied. At surface (3), (4), (5), (6), and (7) the temperature input signals were applied. (For interpretation of the references to colour in this figure legend, the reader is referred to the web version of this article.)

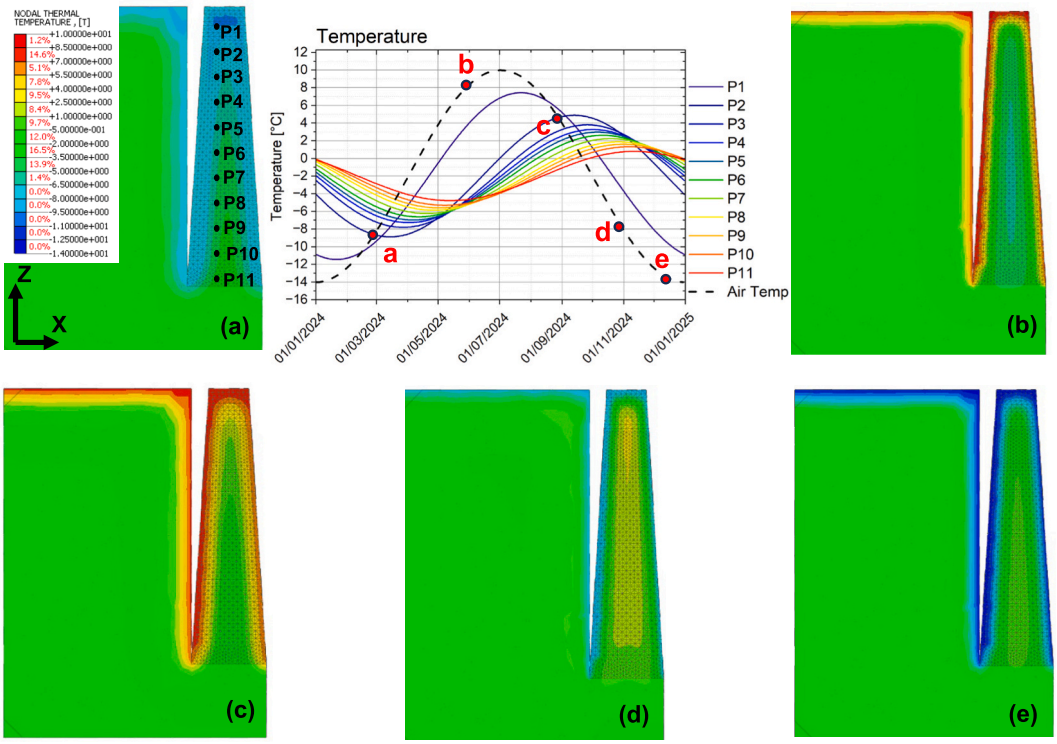

Fig. 5. Numerical results for simulation with the homogeneous external temperature: (a-e) Pillar geometry cross section showing the temperature distribution at different time instants during the year. Figures (a, c) represent the minimum and maximum air temperatures, respectively; other figures (b, d, e) are intermediate values. In the plot the input sinusoidal air temperature (dashed line) and the temperature for 11 different points along the central vertical of the pillar, are represented (continuous lines).

initial condition, the temperature evolution stabilized and became consistent for all subsequent years. Given the relatively small dimensions of the pillar compared to the surrounding model box, temperature variations within the pillar are predominantly controlled by the boundary conditions rather than the variation within the model box. The model box, however, generated a thermal inertial effect, accumulating heat during the summer and releasing it during colder seasons. Temperature inhomogeneity within the pillar led to corresponding inhomogeneities in the strain and stress fields, resulting in non-uniform displacements (Fig. 6). Macroscopically, this inhomogeneity cause a deflection of the pillar, with top points moving in the x direction. As this inhomogeneity varied with time, the deflection also varied throughout the year, ranging from $+0.002m$ and $-0.004m$. Furthermore, during cold months, warmer temperatures are observed inside the pillar compared to sub-zero ambient air. Conversely, during the warm months, the central body of the pillar exhibited temperatures above $0^{\circ}C$. This phenomenon generates a seasonal expansion in warm months, followed by contraction during winter (Fig. 6). Hence, during winter, the pillar appeared smaller compared to its initial size (indicated by black borders in Fig. 6), a reduction attributed to contraction caused by the low temperatures. A similar effect was observed in spring when the cold thermal front reaches the pillar center. Conversely, in summer and autumn, the pillar appeared larger than its original shape due to thermal expansion. It is important to note that the observed deformations are measured in millimeters and have been visually amplified in the figures to enhance clarity and to demonstrate the movement.

Subsequently, a new simulation was carried out to model the effects of temperature differences between two pillar faces, specifically addressing the north face lower exposure to solar radiation compared to others. The pillar lateral surfaces were categorized based on imposed boundary conditions. For faces (3), (5), and (6) (surface encircled in Fig. 4), the same boundary condition from the previous analysis was applied. For surfaces (4) and (7), a vertical temperature gradient with elevation was imposed (Fig. 5), ranging from −1 °C at the top of the pillar to −4 °C at the base, with a linear variation between these two extremes and this gradient was added to the temperature function imposed to the surfaces (3), (5) and (6).

The imposed thermal gradient resulted in an asymmetric temperature field relative to the vertical plane, which, in turn, generated an asymmetry in the deformational response. Notably, portions of the pillar subjected to higher temperatures exhibited more pronounced thermal expansion than cooler zones, leading to differential deformation across cross-sections (Fig. 7d and e). This induced a mechanical response characterized by torsional behavior of the entire pillar, with progressive rotation of the structure longitudinal axis. In all graphs presented in Fig. 5, Fig. 6 and Fig. 7 showing temperature and displacement for points P1-P11, the dashed line represents the sinusoidal air temperature input used during the simulations, while the continuous line represents the time series of these variables for each investigated point.

3.2.2. *Convex rock wall*

The second simplified geometry features a convex face (Fig. 8), reproduced by a half-truncated cone. This half-truncated cone is rigidly connected at both its base and back side to a surrounding model box, ensuring the system behaves as a single body. The surrounding model box, while geometrically similar to the previous case study, has larger dimensions (Fig. 8). To reduce computational time, only half of the domain was utilized due to symmetry. A sensitivity analysis was conducted to determine the optimal extent of the surrounding domain. This domain needed to be sufficiently large to avoid boundary effects while limiting computational cost. Consequently, a width of 275 m was chosen. The simulation mesh consists of 36,492 elements and 7275 nodes. The material is linear, elastic, isotropic and its properties correspond to Set01 (Table 1). The following boundary conditions were imposed: displacement constraints were applied along the z-direction on surface (2), the x-direction on surface (3) and (4), and the y-direction on surface

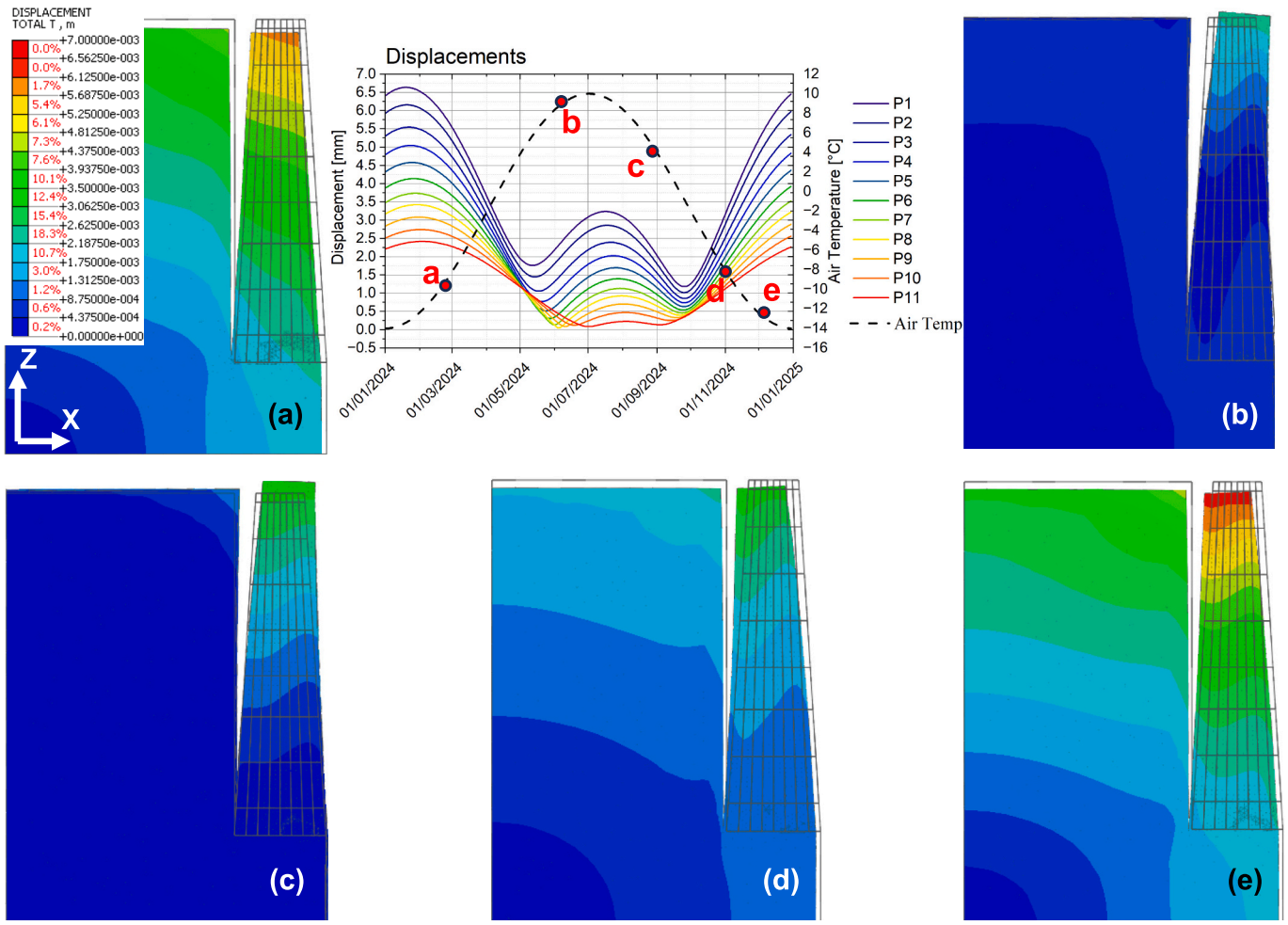

Fig. 6. Numerical results for simulation in which the homogeneous external temperature is imposed displacement at different time instants (corresponding to those in Fig. 5). The graph shows the total vertical displacement for points P1 to P11 together with the imposed external air temperature.

(1) (see Fig. 8). Convective boundary conditions were applied to all surfaces except surface (1), (2), (3) and (4), where a heat no-flux condition was imposed.

The initial temperature was set to 0 °C, and the system was subjected to gravity. Due to unknown site-specific conditions, and the potential influence of initial conditions on numerical simulation results, the system was brought to a thermal steady-state. This was achieved by applying a sinusoidal thermal boundary condition over an initial long period of 40 years. After that displacements were clear and other two years of simulation were carried out with an external temperature following the function reported in Fig. 10b.

The temperature results for this model are consistent with those observed in the previous analysis, showing the thermal front propagating into the domain with a delay relative to the input signal. However, the thermal inertia, although always present, acts in different way from that described in the previous simplified geometry. Indeed, in this case the domain of interest forms a unique body with the surrounding box without any gap in which two boundary conditions could be imposed on two sides.

Displacement time series considering only the period after the steady state, were examined. The displacement time series demonstrated that variations along the z-direction are not significant (Fig. 9). This is because the ~~thickness~~ depth of temperature variation within the domain is uniform along the altitude. Finally, displacements were plotted for points on the convex surface located at the same elevation (Fig. 10). Displacements were highest in the central frontal region of the half-truncated cone and progressively decreased laterally away from it, with the outermost points, close to the surrounding model box, exhibiting the smallest values. The maximum displacement occurred in summer with a value of approximately $+0.3mm$ at the central area. The ratio between the vertical component of the displacements (displacements in the $z-axis$, V) and the horizontal component ($H = \sqrt{x^2 + y^2}$) was calculated to assess the dominant displacement component. The obtained V/H values range from 0.43 to 0.51, indicating that vertical displacements represent 40–50% of the horizontal displacement, as shown in Fig. 10d.

3.3. Topography generation for the real case study

Although the preceding simulations employed simplified geometries, they provided valuable insights into the system response to cyclic thermal loading. These models facilitated clear visualization and comprehension of how external temperature variations impact cliff behavior over time. Building on this foundation, more complex analyses were conducted on real geometries, progressively incorporating additional parameters such as slope orientation to replicate natural conditions. The outcomes of these simulations were directly compared with ground-based radar data, which were processed to isolate the thermally induced cyclic component of displacement. This comparison served a dual purpose: firstly, to validate the numerical models, and secondly, to quantify the thermal signals detected by remote sensing techniques, thereby enhancing the understanding of rocky cliff monitoring data and thermal mechanical response. To achieve these results, a specific procedure was employed for generating the real topography.

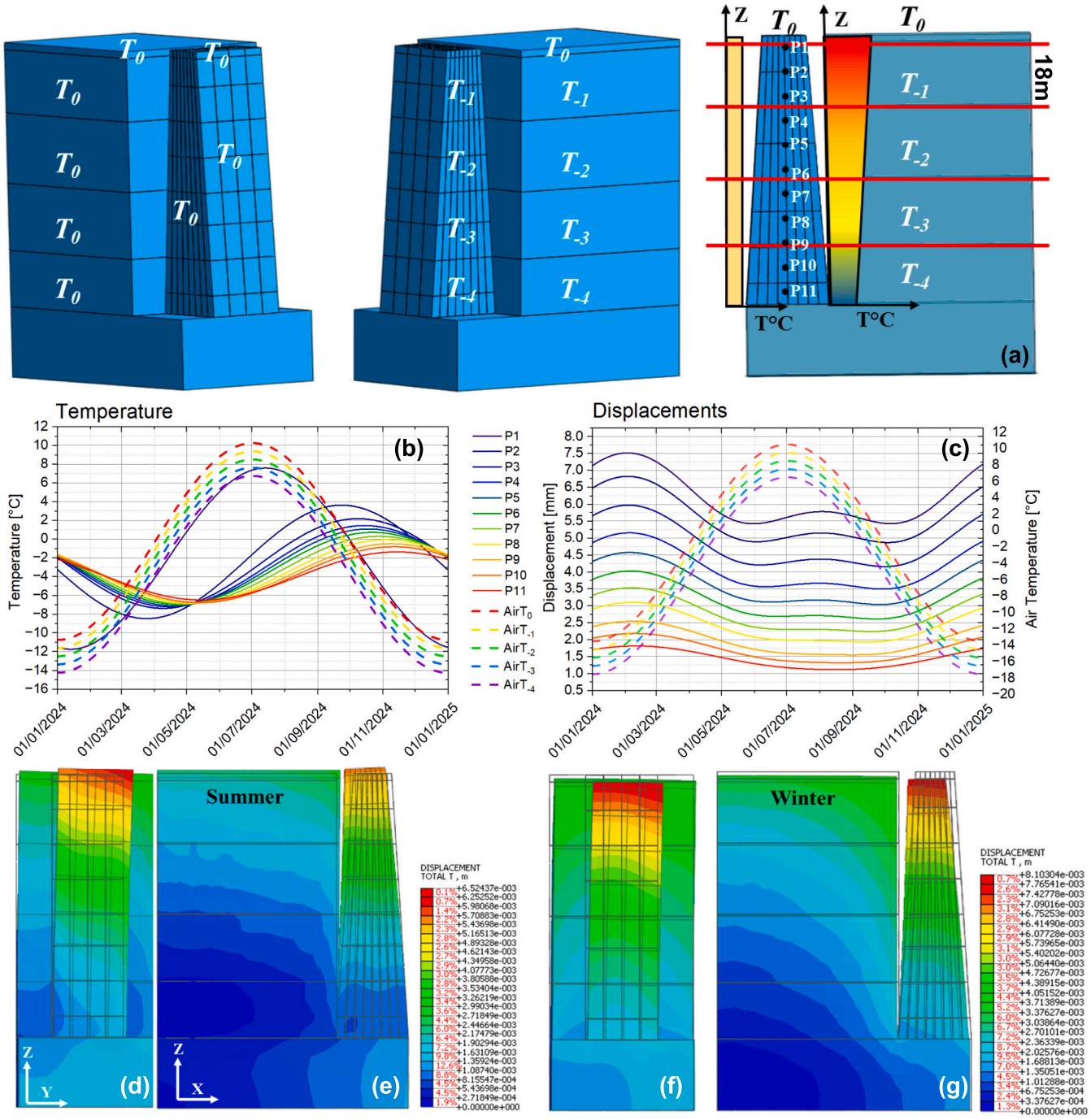

Fig. 7. Different air temperature time series as a function of face exposure(a) applied to domain. Total displacement results for: (d) Frontal view during summer season; (e) Lateral view during summer season; (d) Frontal view during winter season; (g) Lateral view during winter season. The graphs show: (b) Temperature distribution for the same points (as in Fig. 5); and (c) corresponding displacement.

Defining the actual geometry of the study area is a crucial step to ensure consistency between the numerical model and the expected behavior of the real system. In this work, the three-dimensional geometry of the investigated slopes, Monte Scaiùn and Monte Colodri, was constructed based on high-density LiDAR point clouds. These point clouds initially included elements irrelevant to the analysis, such as vegetation or temporary man-made structures. The raw point clouds comprised a total of 26,740,890 points (with a resolution of 10*cm*) for Scaiun and 6,680,884 points (with a resolution of 20*cm*) for Colodri. To enhance the accuracy of the topographic model and minimize geometric distortions in the subsequent numerical modeling, the point clouds underwent preliminary processing using CloudCompare©. During this phase, a selective cleaning removed points associated with dense vegetation, which could compromise the quality of the interpolated topographic surface. Once filtered and homogenized, the point clouds were used to generate a Digital Terrain Model (DTM). This DTM ensured a continuous surface suitable for numerical modeling and reduced the impact of potential discontinuities in the raw point data. The spatial resolution of the DTM was set at 2 × 2 m, considered an optimal compromise between geometric detail and computational manageability within the finite element modeling software. From the resulting DTM, contour lines with a vertical spacing of 5 m were derived,

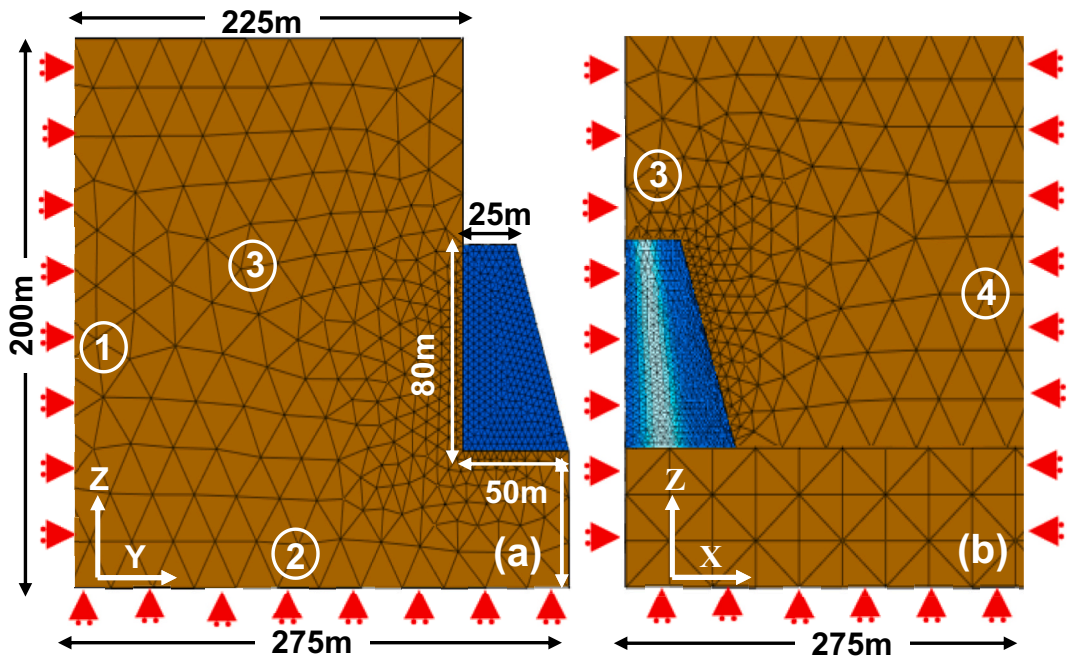

Fig. 8. Geometry and mesh of the simplified convex rock wall shape used in the analysis: (a) Lateral view; (b) Frontal view. The mesh size of the convex shape is 2 m, and for the rest of the domain, it varies up to 20 m. Numbers indicate the faces where boundary conditions were applied.

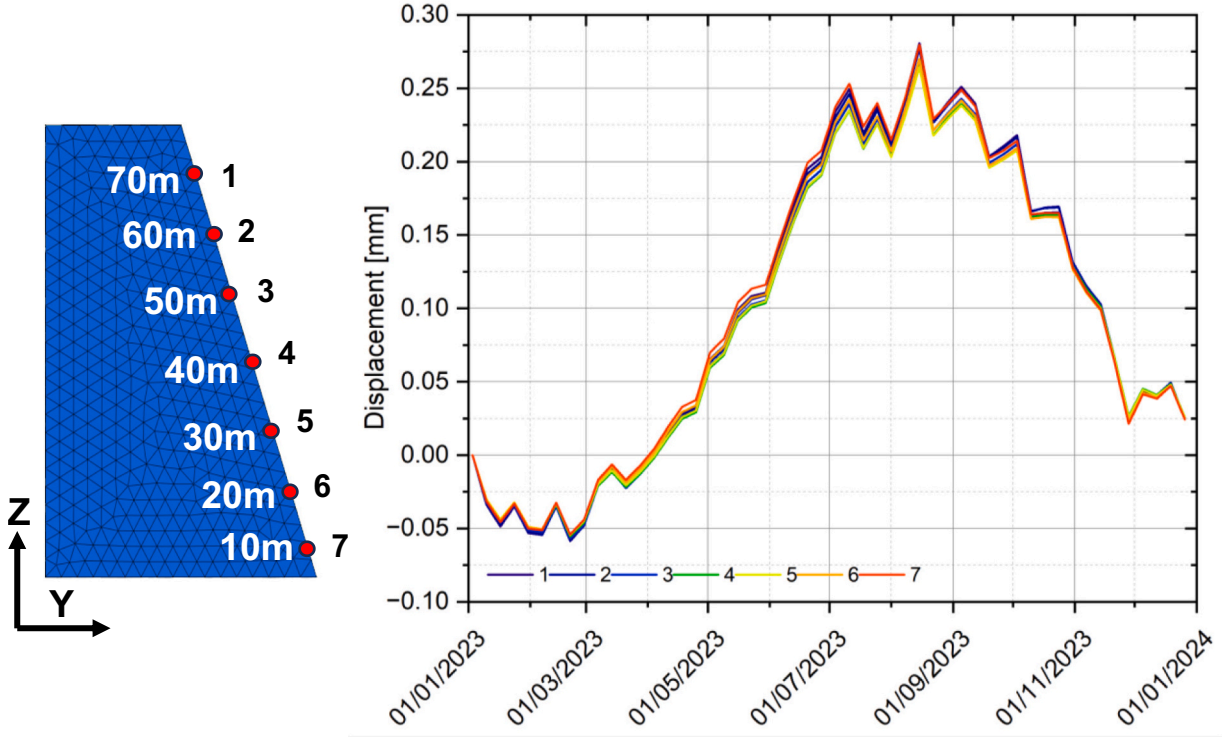

Fig. 9. Time series of displacement during one year of simulation along different *Z*-position in the central part of geometry.

exported, and subsequently used as the basis for generating the external surface of the domain in MIDAS FEA NX. This meticulous process yielded a three-dimensional surface that faithfully reproduces the morphology of the slope, serving as the geometric foundation for the subsequent steps of meshing and definition of boundary conditions.

3.4. Simulations of real case studies

3.4.1. Scaiùn cliff

The mesh used for the Scaiùn cliff analyses comprises 95,770 elements and 19,118 nodes. Similar to simplified geometry analyses (the half-truncated cone cliff), a thermal input was applied to the external surface to replicate annual variations in ambient air temperature. The initial temperature of the domain was set to $-12^{\circ}C$, corresponding to

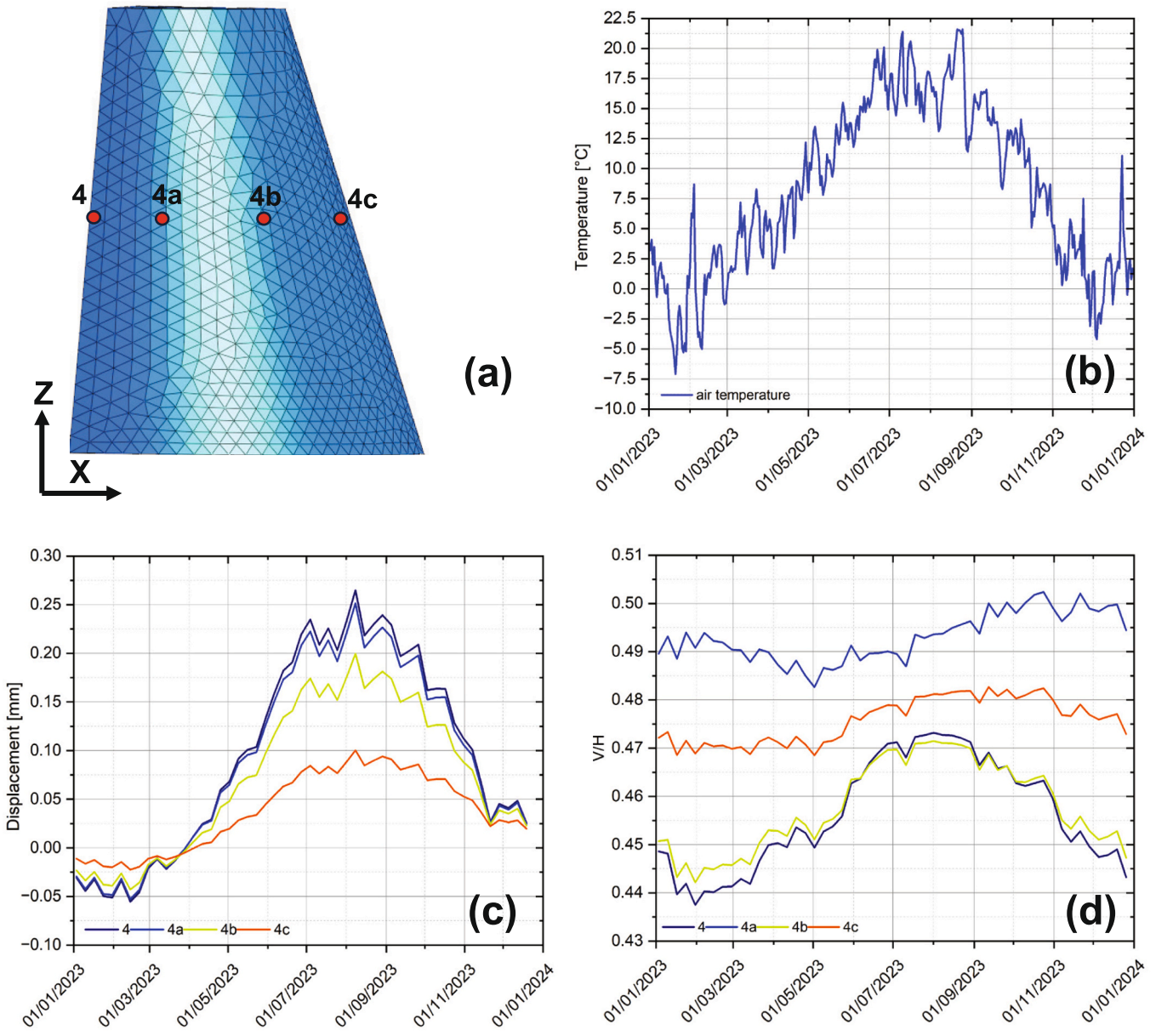

Fig. 10. (a) Control points along the convex surface at a fixed Z-elevation; (b) Time series of air temperature adopted for Scaiun case for the year 2023; (c) Total displacement time series for each control point; (d) V/H (vertical-to-horizontal displacements) ratio.

the first value of the thermal input sine wave. This choice was made to prevent excessively high stress levels at the simulation commencement due to the difference between the initial conditions and the initial value of the boundary condition, which could have adversely affected the displacement outcomes by distorting the thermal and mechanical behavior of the system. Displacement constrains were applied in the coordinate directions and corresponded to no-flux boundary conditions on specific surfaces, consistent with the previous simplified geometry analyses. Two types of analyses were conducted: thermal elastic analyses with uniform thermal input and non-uniform thermal input considering surface exposure. For the latter, two distinct air temperature time series were applied to the North and South faces, respectively, with a 10 °C difference, to simulate the effect of solar radiation. To assess the face orientation, a MATLAB code was developed to calculate the normal vectors of the mesh elements faces (Fig. 11a). In all the analyses the material proprieties were those for Set 02 (Table 1) and represent parameters of a fractured rock mass modeled as a homogeneous continuum (Carlà et al., 2021; Marmoni et al., 2020; Mufundirwa et al., 2011), under the assumption that discontinuities, especially close to the cliff faces, are homogeneously distributed in the domain, and a gravity force was applied to the entire domain. The results regarding uniform temperature generalize the same conclusions obtained for the simplified geometry and therefore it is not considered here. Consequently, we discuss only the case with non-uniform input temperature.

The face with southern exposure systematically exhibited higher temperatures due to increased solar radiation input. This non uniform thermal boundary condition induced a non-uniform temperature gradient across the domain, which, in turn, influenced the internal temperature distribution (Fig. 11b). As a direct consequence, the resulting displacement field was also affected, showing greater deformation in regions exposed to higher thermal loads (Fig. 11c).

3.4.2. *Monte Colodri*

The same procedure as for the Scaiùn cliff case was applied here. The mesh represents a large area and was therefore divided into different parts to limit computational cost, comprising 82,983 elements and

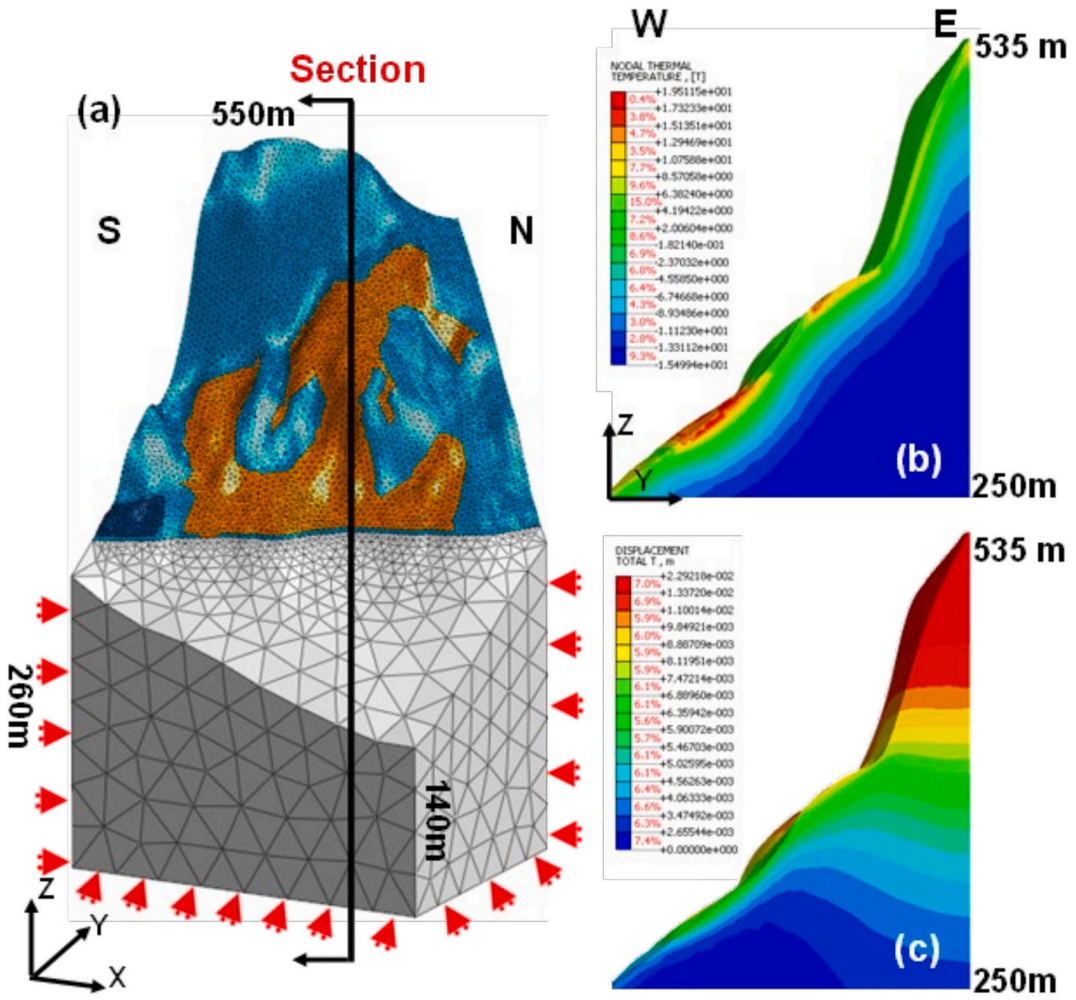

Fig. 11. Numerical simulation results with non-uniform thermal input: (a) Scaiun mesh used for analyses and section (black line) (b) and (c) temperature and displacement distributions in the section, respectively, at winter season.

15,201 nodes. In this case, too, the temperature input was derived from a meteorological station close to the area and adjusted to the correct elevation before being applied to the external surface. The initial temperature for this model was set to $0^{\circ}C$. The procedure for all the analyses (thermal elastic with and without orientation effects) remained consistent to the previous analysis: an initial long period to reach a steady state, cleaning of displacements, followed by a period to quantify displacements induced by thermal loads. Similar to the Scaiùn case, the temperature input difference between the North and South face was $10^{\circ}C$. Displacement constraints were applied along $z-axis$ to surface (2), $x-axis$ to surface (3), and $y-axis$ to surface (1) (Fig. 12a and b). These constraints correspond to no-flux conditions. Gravity force was applied to the entire domain, and the material proprieties are those of Set 02 (Table 1). The temperature distribution is shown in Fig. 12c along a vertical section (Fig. 12b). The temperature distribution evidences the influence of face orientation, demonstrating asymmetry with the southern part being warmer than the northern part. This distribution, consequently, influences the displacement field (Fig. 12d), with major displacements occurring in ~~the~~ southern facing slopes, which expand more than the northern faces with same direction. Hence, a stretching of the model box and of the cliff occurs.

3.5. Data elaboration and model validation

3.5.1. Scaiun cliff

As depicted in Fig. 2(b), the observed displacement along the LOS exhibits a trend characterized by the superposition of two phenomena: a progressive increasing trend attributed to the accumulation of damage and/or irreversible (plastic) strains, and a cyclic variation induced by temperature fluctuations. Given that this study focuses exclusively on thermally induced effects, displacements resulting from damage and irreversible strains were filtered from the in-situ measurements. To achieve this, a detrending procedure was applied to the in-situ displacement data to isolate the seasonal component of the displacement signal. This involved performing a linear interpolation between data points corresponding to the same calendar date across consecutive years (e.g., January 1, 2024, and December 31, 2024). This interpolated line, representing the non-seasonal long-term trend, was then subtracted from the original data, effectively isolating the seasonal displacement component. The detrended data were subsequently compared with the results from the thermo-elastic numerical model. This comparison revealed good agreement in the general temporal evolution of displacements, with both datasets (calculated and measured) displaying a similar waveform (Fig. 13). Nonetheless, a slight phase shift was observed, where the simulated displacement signal slightly anticipated the peak of positive displacements relative to the field measurements. This phase shift was also reflected in the timing of the winter contraction phase, where the differences are more marked. This discrepancy can be mainly attributed to the modeling assumptions regarding thermal input. The first one is that temperature variation was imposed using a sinusoidal function peaking around mid-July. However, meteorological records for the reference year indicate that the actual maximum air

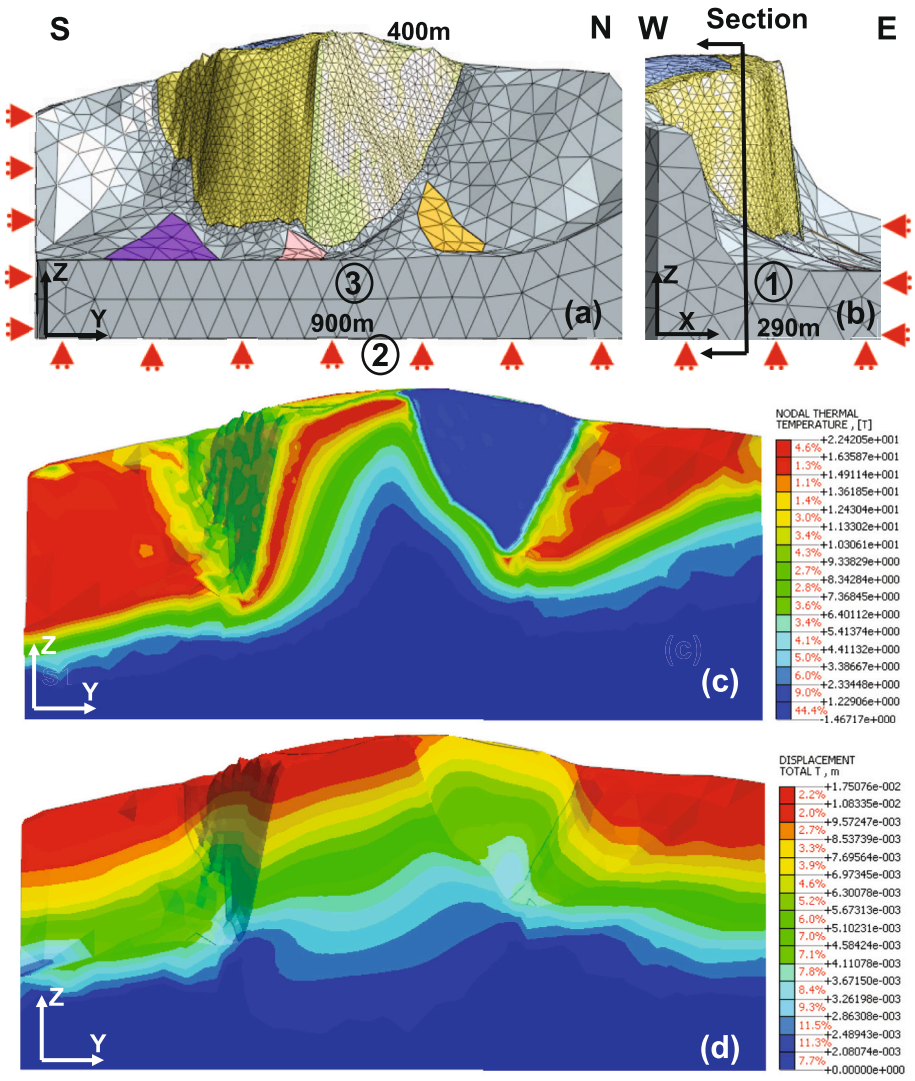

Fig. 12. Monte Colodri numerical results at winter season with aspect effect (a) and (b) mesh in frontal and lateral view, respectively with a vertical section (black line); (c) temperature distribution along the section and (d) displacement distribution along the section.

temperatures occurred in August, leading to a delayed thermal response in the rock mass. Secondary, the described detrending procedure may not have completely removed all the effects induced by damage and irreversible strains. In terms of displacement magnitude, quantitative differences were identified between the simulated and measured data. These differences are anticipated, given the qualitative nature of the numerical model, which was not calibrated for precise displacement amplitudes but rather aimed at capturing the general behavior of the system under purely thermal loading. In this framework, the detrended seasonal signal is interpreted as a predominantly thermo-elastic response to temperature forcing, which is the component explicitly reproduced by the thermo-mechanical model. The residual long-term trend is instead taken to represent irreversible deformation driven by gravitational and time-dependent processes that are not included in the present elastic formulation. Repeated seasonal thermal cycles may still contribute to progressive damage and creep, and thus indirectly to the long-term trend, but this potential coupling cannot be quantified with the available monitoring record and the purely elastic modeling approach adopted here. Finally, other factors such as hydrological effects, external loads, or lithological heterogeneities were not included in the simulation and may further contribute to the observed discrepancies.

Using the results from numerical modeling, displacement maps were reconstructed to emulate the typical outputs generated by processing ground-based interferometric radar data. For a fixed time instant, viewpoint, and viewing direction, these maps represent a spatial surface displacement field of the monitored rock wall. To better capture the deformation behavior along the LOS, maps were generated from three viewpoints: one central (mimicking real instrument position) and two lateral perspectives (Fig. 14). This approach accounts for the fact that when monitoring steep rock walls, the perceived displacement of a given point can vary significantly depending on the sensor viewing geometry and its alignment with the actual movement direction. The displacements of the final day simulated in the previous year was selected as the initial reference for calculating relative variations induced by subsequent seasonal thermal changes (i.e. the displacement of a point at a generic time is the difference between its current displacement and its displacement at the initial reference). The analysis indicates that displacements are negligible during the early months of the year. As temperatures rise towards the summer, a progressive expansion of the rock wall is observed, consistent with the patterns detected in the time series (Fig. 14). In the subsequent months, as temperatures decrease, the wall gradually contracts, returning towards its initial configuration. These generated maps enable detailed tracking of the slope dynamic response to seasonal thermal forcing, offering valuable insights into the observed deformation mechanisms.

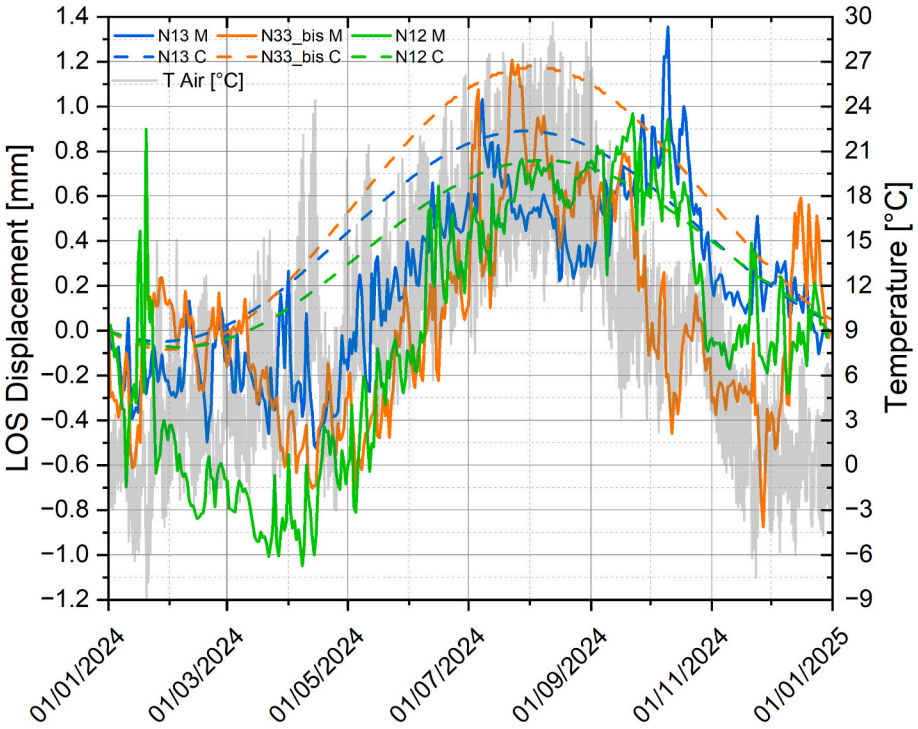

Fig. 13. Comparison of displacement time series along the LOS for the Scaiùn cliff: in-situ measurements (solid line, with suffix M) versus calculated displacements (dashed line, with suffix C). The grey line represents the air temperature.

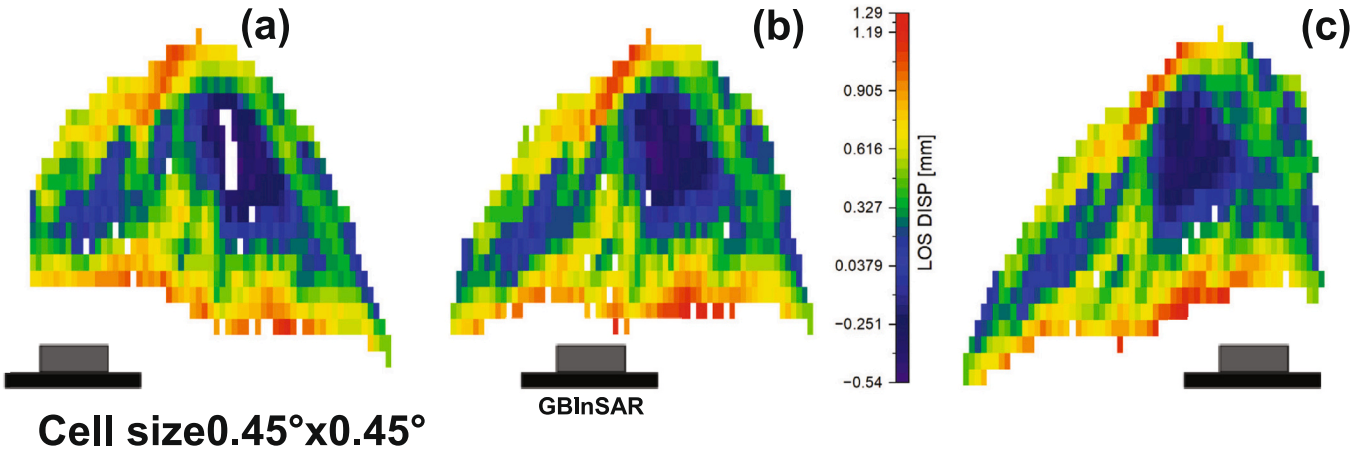

Fig. 14. Scaiùn map of displacement along LOS for the month of July, presented from different viewpoints: (a) left side; (b) frontal; (c) right side. Grey shape indicate the position of radar.

3.5.2. *Monte colodri*

To comprehensively describe the temporal evolution of the Monte Colodri rockwall deformational response under thermal variation, displacement maps derived from the FEM results were generated. These maps (Fig. 15) represent four distinct months, corresponding to the main seasons of the year. Consistent with previous definitions, the reference time for computing displacements was set as the last day of simulation from the preceding year. During the initial month, January, representing a short-term interval from the reference time and characterized by low temperatures, no significant displacements are observed. As warmer months approached, a progressive activation of deformational behavior was detected, aligning with the increase in temperature. Specifically, the south-facing sector of the wall underwent greater thermal expansion, resulting in LOS displacements moving away from the sensor and reaching values up to 2 mm. In contrast, the northern portion exhibited positive displacements, likely influenced by the mechanical response induced by the expansion of the southern sector, which generated local effects in the adjacent rock mass. As the system transitioned into the autumn and winter seasons, characterized again by decreasing temperatures, the wall gradually returned towards its initial configuration: the thermal contraction led to a reduction of the displacements observed during the warmer months, delineating a seasonal cycle consistent with the elastic behavior imposed by the numerical model.

3.6. *Parametric analyses*

To investigate the effects of the main thermo-mechanical parameters on the system response, a parametric analysis was conducted on a Scaiùn cliff FE mesh with a reduced number of nodes. These simulations were performed by individually varying each parameter from the reference

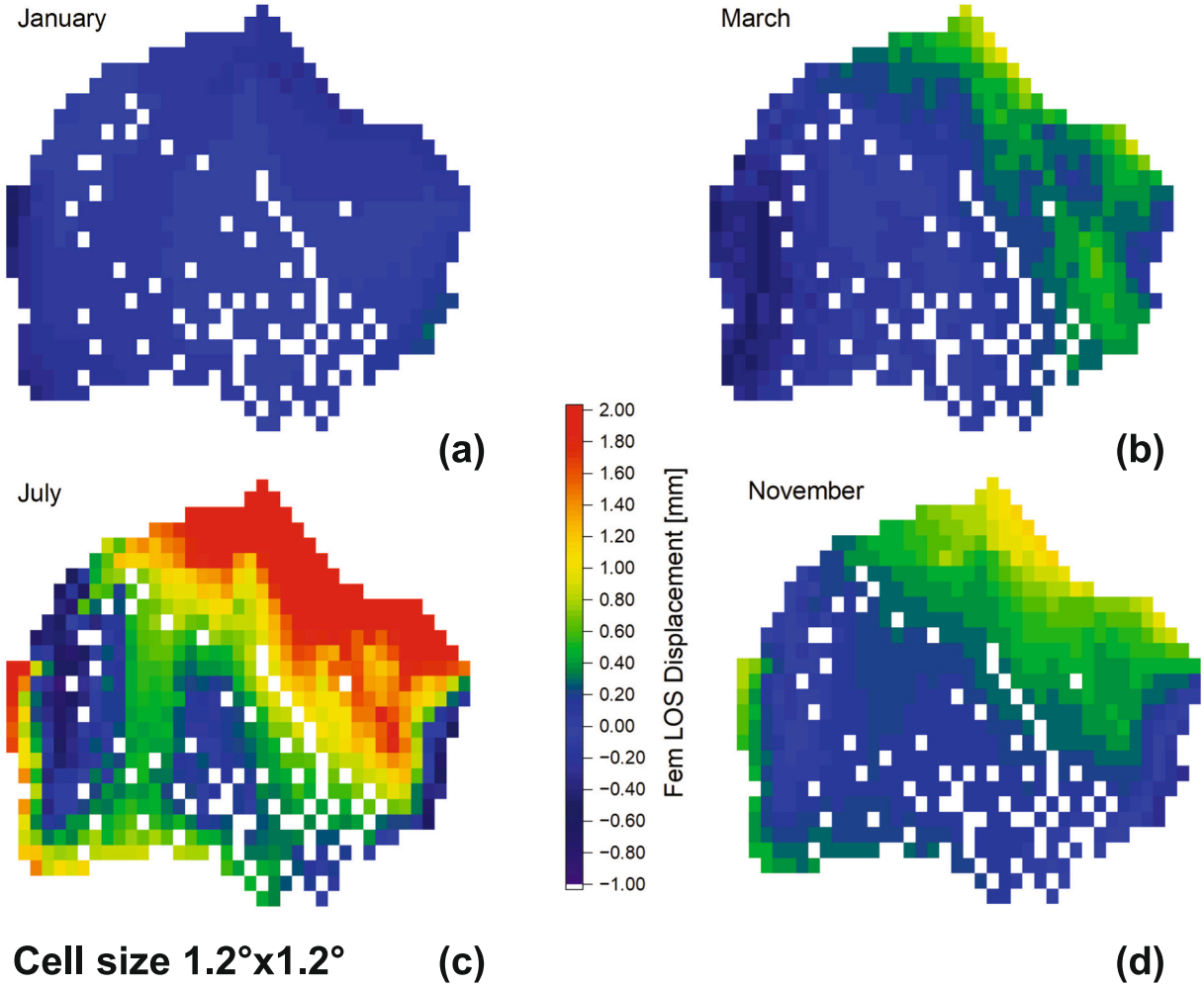

Fig. 15. Monte Colodri map of LOS displacement calculated from FEM simulation at different months: (a) January; (b) March; (c) July; (d) November.

set (Set 02 in Table 1), while keeping all other parameters' values constant. Table 2 provides a list of the numerical simulations included in this set of analyses with the parameter values employed in the simulations.

Fig. 16 presents the results in terms of displacement and vertical stress fields for each simulation, focusing on a single mesh node. Each subgraph in Fig. 16 illustrates the impact of varying a single parameter relative to the reference settings: (a) Young's modulus, (b) specific heat, (c) thermal conductivity, and (d) thermal expansion coefficient.

The analysis revealed distinct influences of each parameter on the thermo-mechanical behavior of the system. The elastic modulus (Fig. 16a) affects significantly vertical stress, but this does not substantially alter the distribution or magnitude of displacements, as the induced deformations are primarily governed by the thermal expansion coefficient and the thermal field. It is important to note that if stress variation exceeds the failure condition, changes in stiffness could induce progressive rock degradation.

Table 2
List of performed parametric analyses and values adopted for the parameters together with the refence ones (Set 02). In bold the values changed from the initial ones.

Simulations *ID*	Young's module $[N/m^2]$	Specific Heat $[J/(kg*K)]$	Thermal Conductivity $[J/(m*day*K)]$	Thermal Expansion Coeff. $[1/K]$
Set 02	1.00E+10	900	216,000	5.00E-06
Para_E01	**5.00E+10**	900	216,000	5.00E-06
Para_E02	**1.00E+09**	900	216,000	5.00E-06
Para_K01	1.00E+10	900	**172,800**	5.00E-06
Para_K02	1.00E+10	900	**259,200**	5.00E-06
Para_Cv01	1.00E+10	**500**	216,000	5.00E-06
Para_Cv02	1.00E+10	**1200**	216,000	5.00E-06
Para_CET01	1.00E+10	900	216,000	**2.00E-06**
Para_CET02	1.00E+10	900	216,000	**1.00E-05**

While thermal conductivity governs the rate of heat diffusion within the domain, it was found to have a marginal effect on both displacement and stress (Fig. 16b). Because no modification of the temperature distribution occurs, changes in conductivity do not modify the displacements observed along the line of sight (LOS). Instead, variations in heat diffusion rate primarily influence the time required to reach a given thermal distribution.

The specific heat (Fig. 16c) exhibited a direct influence on the thermo-mechanical response. Higher specific heat values indicate a greater thermal capacity of the medium, meaning more energy is required to induce a temperature increase. This effectively dampens thermal gradients over time, leading to a reduction in the amplitude of induced deformations and, consequently, observable displacements. Conversely, lower specific heat values cause the material to heat up more quickly under the same heat flow, forming sharper and more localized thermal gradients that produce more pronounced displacements without significantly affecting the vertical stress field.

The thermal expansion coefficient (Fig. 16d) exerts the most direct and proportional control over the displacement field. An increase in the thermal expansion coefficient causes an amplification of the thermally induced deformation, increasing its intensity without altering the spatial

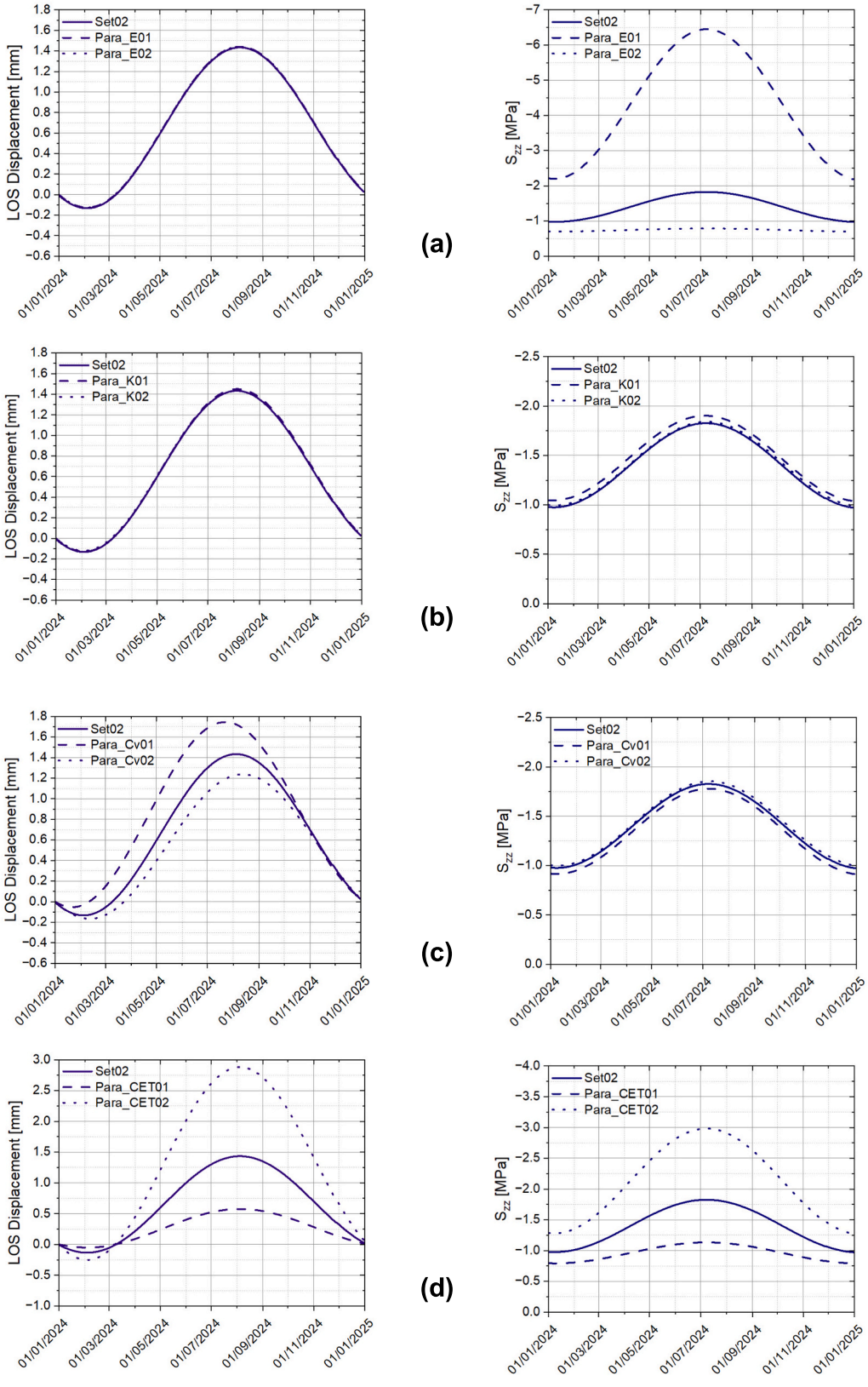

Fig. 16. Results of parametric analyses in terms of displacement and vertical stress for each simulation listed in Table 2, focusing on a single node and at changing: (a) Young's Modulus (E); (b) Thermal Conductivity(α); (c) Specific Heat (Cv); (d) Thermal Expansion Coefficient variation(CET). The values shown in these graphs are extracted in the same position of POI 30 (Fig. 2).

distribution of the displacement field. In this case, the vertical stress field is also significantly affected because increasing the thermal expansion coefficient an increment of the vertical stress peak was observed. We stress that in the analyses an isotropic material was considered.

4. Discussions

Numerical simulations conducted in this study provides a detailed analysis of the thermo-mechanical behavior of rock slopes subjected to seasonal thermal cycles. Despite utilizing continuous medium models, they were parameterized with mechanical properties representative of a fractured rock mass. A key aspect emerging from this work is the crucial role played by geometry, boundary conditions, and slope aspect in controlling both the amplitude and the spatial distribution of stress and strain fields.

4.1. Insights from simplified geometries

Analysis of simplified geometries—specifically the pillar, stocky block, and convex rock wall models—underscores the critical role of morphology in governing the thermo-mechanical response. Understanding these shape-dependent behaviors is paramount for interpreting monitoring data and assessing long-term, fatigue-induced failure risks.

The pillar model, characterized by a high vertical aspect ratio typical of many mountainous areas, exhibited more pronounced vertical displacements at the top, reaching values on the order of $6 - 7$ *mm* when subjected to a real daily air temperature time series. This finding is consistent with the physical principle that, for the same thermal expansion coefficient and temperature variation, taller structures accumulate greater absolute deformations. Similarly, Gischig et al. (2011), modeled the large Randa rock slope instability with a 2D FEM approach, highlighted cumulative and cycling displacements up to $1 - 5$ *mm* at depths of 100 m, with larger deformations concentrated in the less constrained portions of the slope.

Conversely, the curved geometry showed more uniform displacements along the vertical axis but with noticeable lateral variations at the same height. These variations are attributable to the curvature, which localizes the heat flow. These results align with observations by Greif et al. (2017), who reported annual cyclic deformations of $1 - 2$ *mm* in the Pravčická brána natural arch, where stresses and strains accumulate in the curved part of arch, emphasizing the influence of geometry on thermal stress concentration.

From a methodological perspective, the adopted modeling approach incorporated idealized boundary conditions to simulate realistic constraints: fixed displacements at the base representing bedrock anchorage, and free lateral and upper surfaces simulating natural exposure. However, it is important to acknowledge that while these conditions enable the capture of general trends, they may neglect secondary effects related to pre-existing fractures or anisotropies, which are known to locally influence the deformation field and amplify thermal effects at fracture tips.

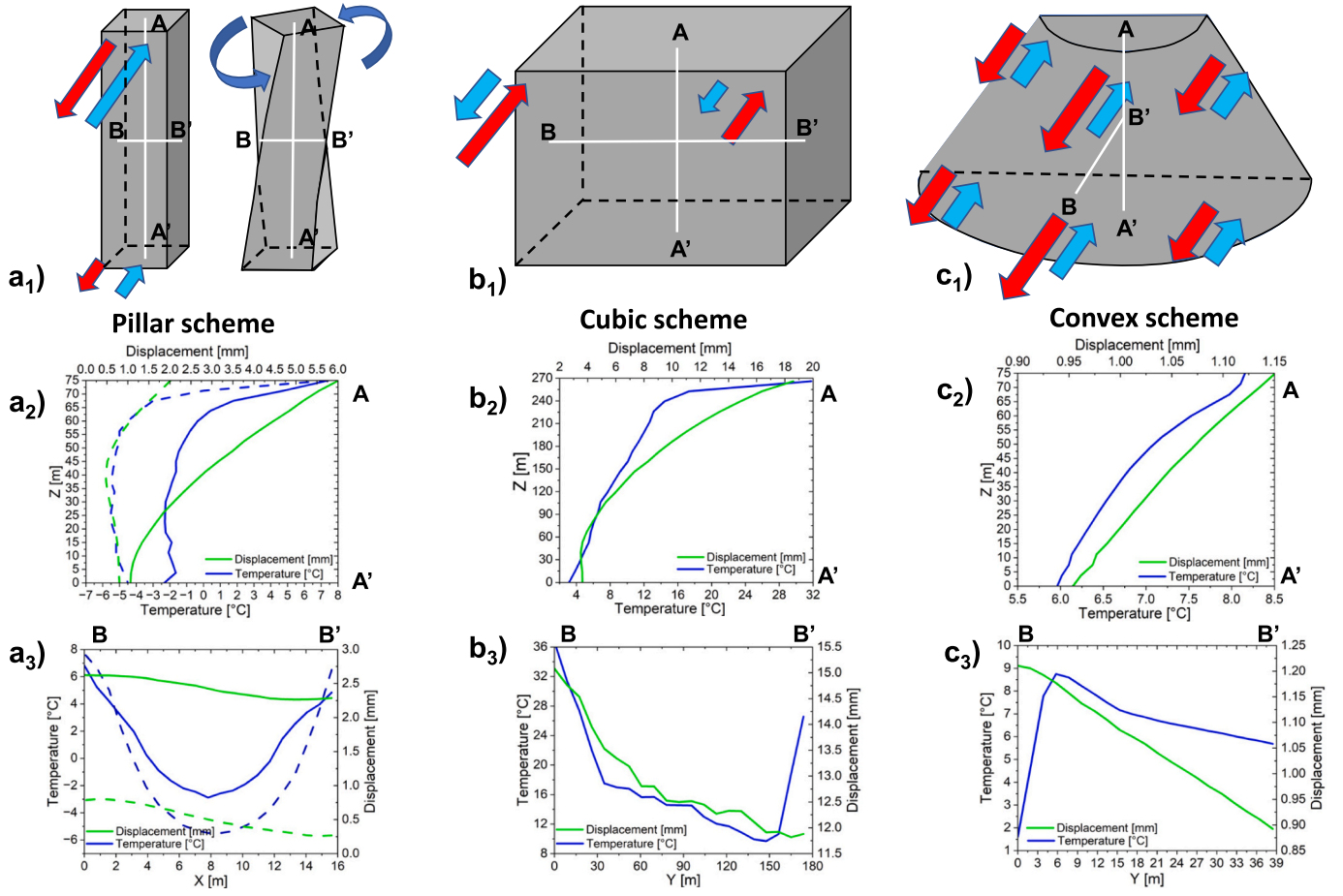

Fig. 17. Sketches and plots of the expected movements for the three main geometries a_1) pillar element with bending and torsional movement, b_1) stocky prism movement, c_1) convex (half-truncated cone) scheme movement; a_2) and a_3) displacement and temperature along the vertical (A-A') and horizontal (B-B′) directions, respectively, for the pillar case (dashed lines for uniform external temperature, continuous lines for non-uniform external temperature), b_2) and b_3) displacement and temperature along the vertical (A-A') and horizontal (B-B′) direction, respectively, for the case of stocky cubic scheme; c_2) and c_3) displacement and temperature along the vertical (A-A') and horizontal (B-B′) directions, respectively for the case of convex scheme.

A particularly notable result from the pillar model, under varying thermal input conditions, was the initiation of torsional deformation, with displacement differences of up to 1.5 *mm* between the exposed and unexposed sides. This finding is in line with experiments by Villarraga et al. (2021), which demonstrated that repeated thermal cycles on limestone samples induce anisotropic degradation of elastic properties and cumulative deformations between 0.1 and 0.5 *mm* after 900 cycles. Although the model used in this study is elastic, the observation that even small temperature differences can produce relevant torsional effects underlines the need to consider such phenomena in real slope monitoring data analysis and stability models.

Fig. 17 illustrates the various types of movement observed in the numerical simulations for both warm (red arrows) and cold (blue arrows) seasons, along with the corresponding displacement and temperature distributions for vertical (A-A') and horizontal profiles (B-B′). For the pillar scheme (Fig. 17 a1, a2 and a3), two subcases were considered: uniform and non-uniform external temperatures. Under uniform external temperatures, a bending movement occurred, characterized by maximum displacement at the top and minimum at the bottom. These displacements were more pronounced in the warm season than in the cold season, with opposite directions. Under non-uniform external temperatures, the pillar was subjected to torsional movement, with displacement magnitudes consistently greater during the warm season. In all warm-season subcases, the internal temperature increased along the vertical direction, while horizontally, it exhibited a convex trend with a minimum in the core of the pillar.

The stocky cubic-like scheme (Fig. 17 b1, b2, and b3) displayed a spatially non-uniform expansion and contraction cycle during the warm and cold seasons, respectively. Specifically, movements on the south-facing side were greater than those on the north-facing side due to differences in external temperature driven by aspect. No significant displacement occurred at the base due to mechanical constraints and the substantial mass. In the warm season, the internal temperature exhibited a quasi-bilinear increase with elevation and a non-symmetric horizontal convex trend influenced by the differing thermal inputs on the north and south faces.

For the convex scheme (half-truncated cone, Fig. 17 c1, c2, and c3), only uniform external temperatures were considered. Here, geometry played a crucial role in controlling the displacement distribution: the magnitude was greatest in the center of the convex surface and progressively decreased laterally. Displacements were more substantial in the warm season, during which the temperature increased with elevation and exhibited a decreasing trend from the external surface inward.

Ultimately, the thermo-mechanical response of idealized geometries acts as a critical diagnostic template for real-world slope behavior. In engineering geology practice, comparing observed GBInSAR displacement patterns against these theoretical models allows for the indirect identification of hidden macro-structural features. For instance, if a seemingly continuous rock face exhibits the thermo-mechanical signature of an isolated pillar or a detached slab, it strongly suggests the presence of deep-seated, persistent rear fractures that kinematically isolate the rock block. Furthermore, incorporating degraded geomechanical parameters demonstrates how the transition from continuous intact rock to a highly fractured mass amplifies displacement magnitudes, altering the thermal signature and aiding in remote slope characterization.

Moreover, our modeling highlights highly localized stress concentrations driven by topographic complexity. From a hazard mitigation standpoint, these geometrical anomalies (e.g., sharp convexities or the upper margins of isolated pillars) represent critical zones where thermal fatigue and crack propagation will predictably initiate. Consequently, these findings provide a physics-based rationale for optimizing the spatial deployment of in-situ monitoring networks (such as extensometers, crack meters, or targeted high-resolution GBInSAR), directing instrumentation precisely to the sectors where thermal stresses peak.

4.2. Model sensitivity

In the parametric analyses, the role of the key parameters was investigated to characterize their individual effects on the displacement and temperature fields and the following considerations can be stated. The elastic modulus predominantly influences the stress field, affecting both its distribution and magnitude, whereas its impact on the displacement field is negligible. This effect on the stress field was also revealed by Gischig et al. (2011), who reported peak-to-peak stress variations of up to ±50% within the range of Young' Modulus they investigated. Thermal conductivity primarily influences the speed at which heat propagates through the domain, with only a marginal effect on displacement and stress fields. Specific heat, conversely, directly influences the displacement field by controlling the thermal inertia of the medium, thereby affecting the distribution of thermal gradient and the sensitivity to temperature changes. It does not, however, significantly impact the stress field. Finally, the thermal expansion coefficient is the only parameter affecting simultaneously the stress and displacement fields, directly controlling the intensity and extent of the overall thermo-elastic response, and as a consequence could be also analyzed by considering anisotropy.

4.3. Applicability to real geometries

In simulations of real geometries, particularly for the Monte Colodri site, the analysis successfully reproduced the expected seasonal trend of Line-Of-Sight (LOS) displacements, with maximum values up toIn simulations of real geometries, particularly for the Monte Colodri site, the analysis successfully reproduced the expected seasonal trend of Line-Of-Sight (LOS) displacements, with maximum values up to +2 *mm* in the south-facing portion. This behavior is consistent with high solar exposure and perfectly aligns with GBInSAR monitoring data. The comparatively smaller displacements observed in the northern portion underscore the critical importance of exposure-driven thermal gradients. This is consistent with observations by Collins and Stock (2016), who documented daily fracture openings of up to1.27 *cm* on sun-exposed granite exfoliation, and Mufundirwa et al. (2011), who reported daily openings of up to 0.21 *mm* even under modest temperature variations Remarkably, the behaviors observed in the idealized pillar model are directly applicable to these complex natural slopes. At Monte Colodri, despite its intricate overall morphology, the southern sector features conspicuous protruding rock masses that kinematically and morphologically behave like isolated pillars. Due to their vertical elongation, partial isolation, and enhanced solar exposure, these structures are subjected to boundary conditions and thermal loads highly analogous to those simulated in our idealized models. Hence, the displacement patterns observed in the simulations, including amplified vertical expansion at the crest and torsional deformations driven by differential heating, can be reasonably anticipated in these natural sub-structures. This correspondence reinforces the interpretative value of the idealized models, demonstrating that they effectively capture fundamental physical processes transferable to real-world scenarios. Because pillar-like morphologies locally amplify thermo-mechanical effects, they must be explicitly accounted for in slope-scale numerical simulations and hazard assessments.

Of particular interest is the heat accumulation effect observed behind the base of the idealized pillar. In this geometric transition zone, heat concentrates and generates a persistent thermal gradient that locally amplifies deformations. This demonstrates that heat primarily accumulates within the shallowest subsurface layers, penetrating and concentrating within the first few meters of the domain. This aligns with Mamot et al. (2021), whose numerical analysis of permafrost rock slopes revealed that thermal variations significantly impact the first 5–7 m below the surface, driving both progressive displacements and a marked reduction in the Factor of Safety. Although Mamot et al. (2021) employed an explicit discrete fracture approach while the present study

adopts an equivalent continuum model, the remarkable consistency in our results underscores the dominant role of surface heat in the overall deformational response. This strengthens the premise that thermal variations can act as primary preparatory factors for rock slope instability, even in the absence of explicit discrete fractures. However, we acknowledge that the current scarcity of deep thermometric borehole data at lower-elevation sites limits the extensive field validation of these simulated internal temperature profiles.

Ultimately, the ability to predict the pure thermo-elastic response of different morphological features addresses a major challenge in remote sensing applied to slope stability. By quantifying the expected reversible thermal deformation for a given slope geometry and rock mass quality, it becomes possible to systematically clean GBInSAR displacement maps. Removing this cyclic thermal noise strictly isolates the residual, unrecoverable plastic strains, which are the true geomechanical precursors of progressive failure and macroscopic collapse.

4.4. Limitations of the isotropic material assumption

In the numerical analysis we adopted isotropic and homogeneous thermal and mechanical properties (Table 1) a clear simplification of the behavior of many foliated and layered rocks. Numerous laboratory studies have shown that elastic stiffness and strength can vary significantly with orientation in metamorphic rocks, reflecting both crystallographic preferred orientation and foliation-related microcrack fabrics (Johnson and Wenk, 1974). Likewise, marbles and other polycrystalline carbonates display strong anisotropy of linear thermal expansion, with coefficients that differ by factors of ~1.5–2 or more between directions of maximum and minimum dilatation, systematically aligned with rock fabric and crystal orientation (Luque et al., 2010; Siegesmund et al., 2000). Thermal conductivity also tends to be anisotropic in foliated and bedded rocks: measurements on Alpine rocks and fine-grained sedimentary rocks show that conductivity and diffusivity are typically higher parallel to foliation or bedding than normal to it, with parallel values exceeding perpendicular ones by up to factors of ~1.5–3.8 (Labus and Labus, 2018). Neglecting such thermo-mechanical anisotropy is therefore expected to influence primarily the magnitude and local orientation of stress concentrations (e.g. favoring earlier shear or tensile localization along weak fabric-related directions), and to slightly modify the distribution of thermally induced strains and torsion-related stress peaks. However, in the present set of simulations the emergence and overall pattern of stress concentrations are mainly controlled by the geometry of the modeled rock volumes and by the imposed boundary conditions; the torsional stress concentrations observed in the pillar examples represent a specific manifestation of this behavior and are therefore expected to remain qualitatively robust even if anisotropic property tensors were introduced. A fully anisotropic thermo-mechanical formulation, explicitly linked to site-specific fabric and directional property measurements, lies beyond the scope of this first modeling step but represents an important direction for future work.

4.5. Methodological advancements in data representation

The reconstruction of displacement maps from the numerical models reveals that, unlike GBInSAR which provides continuous and high spatial resolution data, the FEM results are constrained by the nodal discretization. Although introducing a limitation in capturing finer local effects, the adoption of a slope-scale domain allowed for the generation of displacement fields comparable to GBInSAR data, thereby improving the readability of the numerical results. This represents a significant step forward compared to studies which used coupled numerical models to simulate rock slope response at small scale and at shallow depth or based on superficial disturbance and measurement.

The generation of LOS displacement maps from the FEM simulations required a post-processing step involving the projection of nodal displacements onto a 2D grid defined in radar coordinates. This grid was constructed by discretizing the azimuth and zenith angle intervals (i.e., the viewing geometry of the radar) into cells of variable size. Each cell aggregates the displacements of all the FEM nodes falling within its angular boundaries, effectively creating a spatial raster representation of the modeled displacements. The dimensions of these angular cells can vary, being either square or rectangular, as shown in the comparative example (Fig. 18). The choice of cell size significantly affects the readability and representativeness of the final maps. Larger cells (e.g., $1.4^\circ \times 1.4^\circ$) tend to flatten the map, smoothing out details and potentially masking local variations, while smaller cells (e.g., $0.45^\circ \times 0.8^\circ$) better capture spatial variability but may result in many empty cells due to the limited number of nodes available in some regions, leading to white gaps. Multiple configurations were tested to identify the optimal compromise between spatial resolution and completeness of the information. This process was particularly important because, in contrast to measurement data, FEM results are inherently limited to the spatial distribution of mesh nodes requiring careful spatial aggregation to be meaningfully compared with radar-derived LOS displacement data. In the case of Monte Colodri, shown in Fig. 18, a $1.2^\circ \times 1.2^\circ$-degree cell size was adopted as the best balance between spatial continuity and resolution, allowing for the reconstruction of a coherent displacement pattern while minimizing the presence of empty areas.

4.6. Comparison with field measurements

The comparison between the measured GBInSAR and FEM modeled LOS displacement maps for both the Scaiun and Monte Colodri sites (Fig. 19) reveals key differences and similarities essential for interpreting the model outcomes. A fundamental distinction lies in the nature of the data: the GBInSAR measurements represent cumulative displacements over time, whereas FEM results reflect instantaneous elastic responses to thermal forcing. This inherent difference also explains potential disparities in the sign of displacement between measured and simulated data, as the numerical model isolates the thermal component, whereas monitored data integrate the total deformation signal, including other mechanical or hydrological influences. As described in Data elaboration, detrending the measured time series to isolate the cyclic component provides a more coherent basis for comparison (Fig. 13). In the Scaiun case, despite the different displacement scales, more accentuated in the measured map due to a longer observation period (January to July), some consistent patterns emerge. Both map types exhibit slightly negative LOS displacements in the central, more stable zone. Concurrently, positive values are concentrated at the base of the slope in the modeled data. This lower-slope anomaly corresponds to a morphological change in gradient, suggesting a geometrically driven amplification of thermal displacement at concave breaks, a phenomenon also visible in the in-situ measurements.

Conversely, for the Monte Colodri site, where both maps refer to a similar time window (October to July) and share comparable displacement scales, the sign of displacement is inverted in the most mobile sectors. This inversion is again attributable to the thermal-only nature of the numerical model. Nonetheless, the spatial distribution of the moving areas demonstrate consistency, with both maps highlighting displacement concentration in the southern exposed portion of the slope. This spatial coherence, despite the conceptual and mechanical simplifications of the adopted FEM approach, confirms the ability of thermo-mechanical models to identify thermally sensitive sectors of rock slopes and supports the interpretation of real slope dynamics based on numerical results.

5. Conclusions

This study demonstrates that thermal fluctuations alone, even without additional triggers like rainfall or seismicity, can induce measurable, millimeter-scale displacements in fractured rock slopes. By employing finite element simulations across both idealized and real-

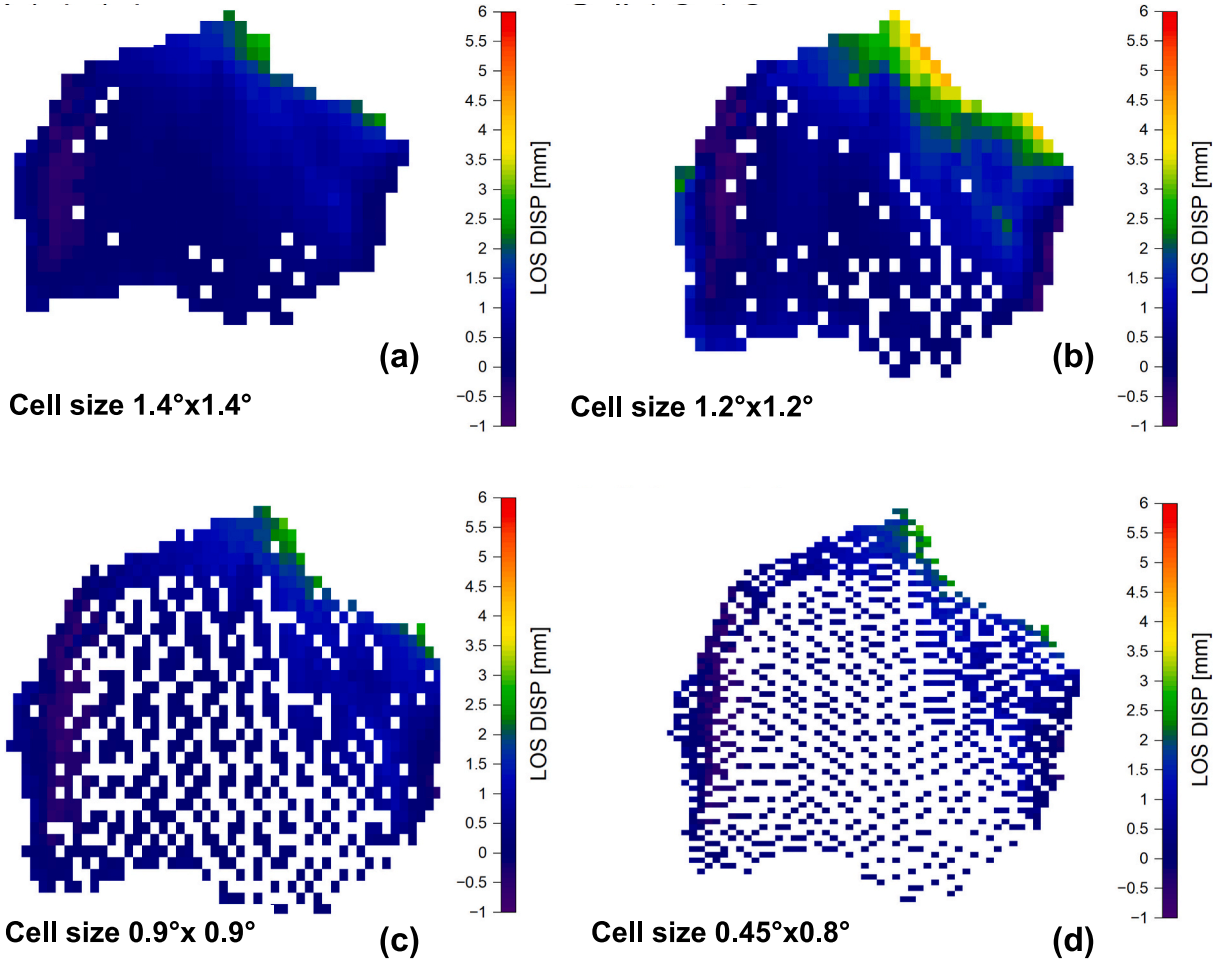

Fig. 18. Comparative example of Monte Colodri LOS displacement maps generated with different cell sizes: from (a) and (b) larger cells (e.g., 1.4° × 1.4°); to (c) and (d) smaller cells (e.g., 0.45° × 0.8°).

world geometries, we show that seasonal expansion and contraction cycles are strictly governed by topographic factors. Specifically, torsional displacement modes in isolated pillars, strain amplification on convex walls, and differential sun-exposed/shaded movements underscore the critical influence of morphology on slope deformation.

By extending the numerical domain to the macro-slope scale, this approach effectively bridges the gap between theoretical thermo-mechanics, large-scale remote sensing (e.g., GBInSAR), and applied engineering geology. Rather than mere theoretical exercises, our models serve as essential diagnostic tools with three primary practical applications. First, they allow practitioners to interpret complex radar displacement maps, enabling the indirect detection of hidden structural releases (e.g., back-fractures) that isolate large rock slabs. Second, because topographic complexities dictate the localization of thermal stresses, these models identify high-stress geometric sectors, allowing for the targeted prioritization of monitoring systems in areas most susceptible to thermal fatigue. Finally, integrating variable rock mass properties provides a quantitative baseline of the expected reversible thermal strain. This baseline is fundamentally required to filter out daily thermo-elastic breathing from radar images, ensuring that early warning systems are triggered by true, irreversible geomechanical damage rather than benign thermal noise.

Ultimately, this study reinforces numerical modeling as a crucial complement to field monitoring, laying the groundwork for developing predictive digital twins of rocky cliffs. Future developments will refine model accuracy by calibrating material parameters with in-situ data and incorporating structural heterogeneities alongside elasto-plastic and fracture propagation mechanics.

Acknowledgments

The authors are deeply indebted to CMG-ARPA Lombardia and Dr. Luca Dei Cas for providing data for the Scaiun case study and Dr. Mauro Zambotto and Geological service of Provincia Autonoma di Trento for the Monte Colodri dataset. Luca Cifeca Recinella received a Ph.D. grant from Piano Nazionale di Ripresa e Resilienza—PNRR "Geosciences IR" Project—IR0000037 (Mission 4 "Education and Research"—Component 2 "From Research to Business"- Investment 3.1, "Fund for the realization of an integrated system of research and innovation infrastructures"—-CUP I53C22000800006) financed by European Union NextGenerationEU is part of project Geosciences funded by PNRR. The research has been partially funded by a Cariplo Foundation grant "Territori Sicuri 2024 for the Project RESILIENT - Risk Evaluation and Smart Implementation of Landslide monitoring by citizen Engagement and New Technologies and the RockLab Project and the PRIN Project – THErmo- and hydro-mechanical monitoring and modeling of jointedROCKs: a national Site Laboratory network (THEROCKLAB)-2022BSFCHK financed by European Union NextGenerationEU.

CRediT authorship contribution statement

Luca Cifeca Recinella: Writing – original draft, Methodology, Investigation, Formal analysis. **Giuseppe Dattola:** Writing – original draft, Software, Methodology. **Carlo Rivolta:** Resources. **Davide Leva:**

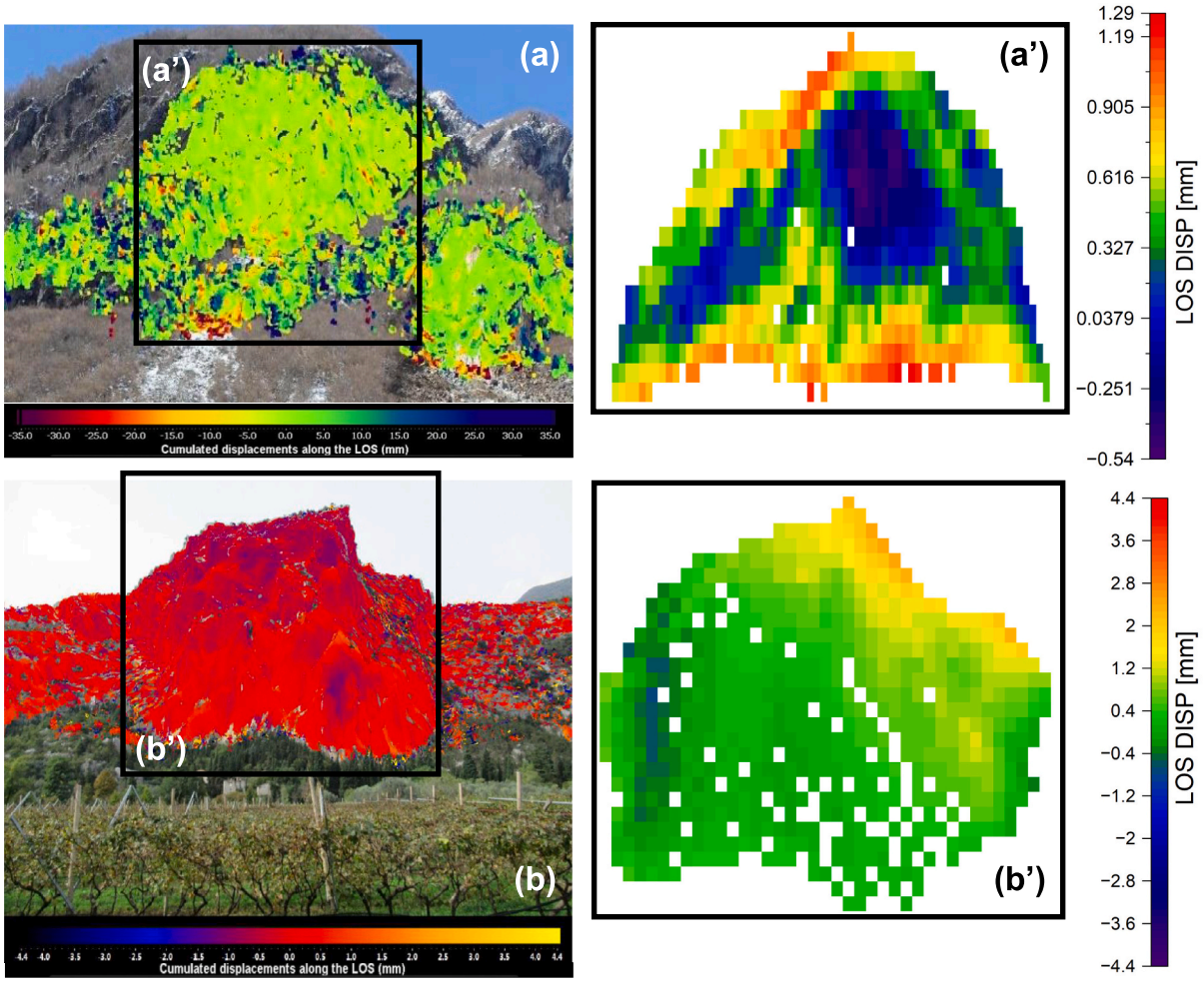

Fig. 19. Comparison between measured LOS displacement maps from GBInSAR (left-hand side) and calculated maps from FEM analysis (right-hand side) for (a) (a') the Scaiùn cliff and (b) (b') the Monte Colodri. The computed maps were prepared using a resolution of 0.45° × 0.45° and 1.2° × 1.2°, respectively, projecting FEM displacements in the LOS direction.

Resources. **Giovanni Battista Crosta:** Writing – review & editing, Supervision, Project administration, Conceptualization.

Declaration of competing interest

The authors declare that they have no known competing financial interests or personal relationships that could have appeared to influence the work reported in this paper.

Data availability

The data that has been used is confidential.

References

Agliardi, F., Crosta, G.B., Meloni, F., Valle, C., Rivolta, C., 2013. Structurally-controlled instability, damage and slope failure in a porphyry rock mass. Tectonophysics 605, 34–47. https://doi.org/10.1016/J.TECTO.2013.05.033.

Bonometti, F.N., Dattola, G., Frattini, P., Crosta, G.B., 2025. Rockfall Triggering and Meteorological Variables in the Dolomites (Italian Eastern Alps). https://doi.org/10.5194/egusphere-2024-4122.

Bourrier, F., Dorren, L., Nicot, F., Berger, F., Darve, F., 2009. Toward objective rockfall trajectory simulation using a stochastic impact model. Geomorphology 110 (3–4), 68–79. https://doi.org/10.1016/J.GEOMORPH.2009.03.017.

Carlà, T., Gigli, G., Lombardi, L., Nocentini, M., Casagli, N., 2021. Monitoring and analysis of the exceptional displacements affecting debris at the top of a highly disaggregated rockslide. Eng. Geol. 294. https://doi.org/10.1016/j.enggeo.2021.106345.

Castellarin, A., Picotti, V., Cantelli, L., Claps, M., Trombetta, L., Selli, L., Carton, A., Borsato, A., Daminato, F., Nardin, M., Santuliana, E., Veronese, L., Bollettinari, G., 2005. Note Illustrative della Carta Geologica d'Italia, Foglio n°80 Riva del Garda. In: Provincia Autonoma di Trento, Servizio Geologico (Issue 5). Libero Professionista.

Clauge, J.J., Stead, D., 2012. Landslides; Types, Mechanisms, And Modeling.

Collins, B.D., Stock, G.M., 2016. Rockfall triggering by cyclic thermal stressing of exfoliation fractures. Nat. Geosci. 9 (5), 395–400. https://doi.org/10.1038/ngeo2686.

Collins, B.D., Stock, G.M., Eppes, M.C., Lewis, S.W., Corbett, S.C., Smith, J.B., 2018. Thermal influences on spontaneous rock dome exfoliation. Nat. Commun. 9 (1). https://doi.org/10.1038/s41467-017-02728-1.

Collins, B.D., Stock, G.M., Eppes, M.C., 2019. Relaxation Response of Critically Stressed Macroscale Surficial Rock Sheets. Rock Mech. Rock Eng. 52 (12), 5013–5023. https://doi.org/10.1007/s00603-019-01832-6.

Crosta, G.B., 1992. An Example of Unusual Complex Landslide: From a Rockfall to a Dry Granular Flow?.

Crosta, G.B., Agliardi, F., 2003. A methodology for physically based rockfall hazard assessment. Nat. Hazards Earth Syst. Sci. 3.

Crosta, G.B., Imposimato, S., Roddeman, D.G., 2003. Numerical modelling of large landslides stability and runout. Nat. Hazards Earth Syst. Sci. 3. http://www.feat.nl.

Dei Cas, L., Luisa Pastore, M., Pavan, A., Petrella, N., 2021. Geological monitoring networks for risk management close to large rock cliffs: the case history of Gallivaggio and Cataeggio in the Italian Alps. Geogr. Helv. 76 (1), 85–101. https://doi.org/10.5194/gh-76-85-2021.

Do Amaral Vargas, E., Velloso, R.Q., Chávez, L.E., Gusmão, L., Do Amaral, C.P., 2013. On the effect of thermally induced stresses in failures of some rock slopes in Rio de Janeiro, Brazil. Rock Mech. Rock Eng. 46 (1), 123–134. https://doi.org/10.1007/s00603-012-0247-9.

Frankovská, J., Kopecký, M., Panuška, J., Chalmovský, J., 2015. Numerical Modelling of Slope Instability. Procedia Earth Planet. Sci. 15, 309–314. https://doi.org/10.1016/j.proeps.2015.08.076.

Frattini, P., Crosta, G., Carrara, A., Agliardi, F., 2008. Assessment of rockfall susceptibility by integrating statistical and physically-based approaches.

Geomorphology 94 (3–4), 419–437. https://doi.org/10.1016/j.geomorph.2006.10.037.
Gischig, V.S., Moore, J.R., Evans, K.F., Amann, F., Loew, S., 2011. Thermomechanical forcing of deep rock slope deformation: 1. conceptual study of a simplified slope. J. Geophys. Res. Earth Surf. 116 (4). https://doi.org/10.1029/2011JF002006.
Greif, V., Brcek, M., Vlcko, J., Varilova, Z., Zvelebil, J., 2017. Thermomechanical behavior of Pravcicka Brana Rock Arch (Czech Republic). Landslides 14 (4), 1441–1455. https://doi.org/10.1007/s10346-016-0784-5.
Gunzburger, Y., Merrien-Soukatchoff, V., 2011. Near-surface temperatures and heat balance of bare outcrops exposed to solar radiation. Earth Surf. Process. Landf. 36 (12), 1577–1589. https://doi.org/10.1002/esp.2167.
Johnson, L.R., Wenk, H.R., 1974. Anisotropy of physical properties in metamorphic rocks. Tectonophysics 23 (1–2), 79–98. https://doi.org/10.1016/0040-1951(74)90112-7.
Krautblatter, M., Funk, D., Günzel, F.K., 2013. Why permafrost rocks become unstable: a rock-ice-mechanical model in time and space. Earth Surf. Process. Landf. 38 (8), 876–887. https://doi.org/10.1002/esp.3374.
Labus, M., Labus, K., 2018. Thermal conductivity and diffusivity of fine-grained sedimentary rocks. J. Therm. Anal. Calorim. 132 (3), 1669–1676. https://doi.org/10.1007/s10973-018-7090-5.
Leva, D., Nico, G., Tarchi, D., Fortuny-Guasch, J., 2003. Temporal analysis of a landslide by means of a ground-based SAR interferometer. IEEE Trans. Geosci. Remote Sens. 41 (4 PART I), 745–752. https://doi.org/10.1109/TGRS.2003.808902.
Leva, D., Rivolta, C., Rossetti, I.B., Kuzuoka, S., Mizuno, T., 2005. Using a Ground Based Interferometric Synthetic Aperture Radar (GBinSAR) Sensor to Monitor a Landslide in Japan.
Luque, A., Cultrone, G., Mosch, S., Siegesmund, S., Sebastian, E., Leiss, B., 2010. Anisotropic behaviour of White Macael marble used in the Alhambra of Granada (Spain): the role of thermohydric expansion in stone durability. Eng. Geol. 115 (3–4), 209–216. https://doi.org/10.1016/J.ENGGEO.2009.06.015.
Mamot, P., Weber, S., Eppinger, S., Krautblatter, M., 2021. A temperature-dependent mechanical model to assess the stability of degrading permafrost rock slopes. Earth Surf. Dyn. 9 (5), 1125–1151. https://doi.org/10.5194/esurf-9-1125-2021.
Marmoni, G.M., Fiorucci, M., Grechi, G., Martino, S., 2020. Modelling of thermo-mechanical effects in a rock quarry wall induced by near-surface temperature fluctuations. Int. J. Rock Mech. Min. Sci. 134. https://doi.org/10.1016/j.ijrmms.2020.104440.
Merrien-Soukatchoff, V., Gasc-Barbier, M., 2023. The effect of Natural thermal Cycles on Rock Outcrops: Knowledge and Prospect. Rock Mech. Rock. Eng. 56 (9), 6797–6822. https://doi.org/10.1007/s00603-023-03420-1.
Mufundirwa, A., Fujii, Y., Kodama, N., Kodama, J.ichi., 2011. Analysis of natural rock slope deformations under temperature variation: a case from a cool temperate region in Japan. Cold Reg. Sci. Technol. 65 (3), 488–500. https://doi.org/10.1016/j.coldregions.2010.11.003.
Noetzli, J., Gruber, S., 2009. Transient thermal effects in Alpine permafrost. Cryosphere 3. www.the-cryosphere.net/3/85/2009/.
Noetzli, J., Gruber, S., Kohl, T., Salzmann, N., Haeberli, W., 2007. Three-dimensional distribution and evolution of permafrost temperatures in idealized high-mountain topography. J. Geophys. Res. Earth Surf. 112 (2). https://doi.org/10.1029/2006JF000545.
Olmedo, I., Bourrier, F., Bertrand, D., Berger, F., Limam, A., 2018. Dynamic analysis of wooden rockfall protection structures subjected to impact loading using a discrete element model. Eur. J. Environ. Civ. Eng. 24 (9), 1430–1449.
Palladino, M.R., Viero, A., Turconi, L., Brunetti, M.T., Peruccacci, S., Melillo, M., Luino, F., Deganutti, A.M., Guzzetti, F., 2018. Rainfall thresholds for the activation of shallow landslides in the Italian Alps: the role of environmental conditioning factors. Geomorphology 303, 53–67. https://doi.org/10.1016/J.GEOMORPH.2017.11.009.
Sarkar, K., Singh, T.N., Verma, A.K., 2012. A numerical simulation of landslide-prone slope in himalayan region—a case study. Arab. J. Geosci. 5 (1), 73–81. https://doi.org/10.1007/s12517-010-0148-8.
Selby, M.J., 1993. Hillslope Materials and Processes. Wiley.
Siegesmund, S., Ullemeyer, K., Weiss, T., Tschegg, E.K., 2000. Physical weathering of marbles caused by anisotropic thermal expansion. Int. J. Earth Sci. 89 (1), 170–182. https://doi.org/10.1007/s005310050324.
Tarchi, Dario, Casagli, Nicola, Moretti, Sandro, Leva, Davide, Sieber, Alois J., 2003. Monitoring landslide displacements by using ground-based synthetic aperture radar interferometry: application to the Ruinon landslide in the Italian Alps. J. Geophys. Res. 108 (B8). https://doi.org/10.1029/2002JB002204.
Valagussa, A., Frattini, P., Crosta, G.B., 2014. Earthquake-induced rockfall hazard zoning. Eng. Geol. 182 (PB), 213–225. https://doi.org/10.1016/J.ENGGEO.2014.07.009.
Villarraga, C., Vaunat, J., Virely, D., Gasc, M., 2021. Effect of thermal cycles on rock cliff deformation. Monitoring and interpretation. IOP Conf. Ser.: Earth Environ. Sci 833 (1). https://doi.org/10.1088/1755-1315/833/1/012152.
Wang, M., Liu, K., Yang, G., Xie, J., 2017. Three-dimensional slope stability analysis using laser scanning and numerical simulation. Geomat. Nat. Haz. Risk 8 (2), 997–1011. https://doi.org/10.1080/19475705.2017.1290696.
Whalley, W.B., 1979. Effect of sand grain shape on interparticle friction; indirect measurements by Rowe's stress dilatancy theory. Geotechnique 29 (3), 341–350.
Woods, A., Macciotta, R., Hendry, M.T., Stewart, T., Marsh, J., 2021. Updated understanding of the deformation characteristics of the Checkerboard Creek rock slope through GB-InSAR monitoring. Eng. Geol. 281. https://doi.org/10.1016/j.enggeo.2020.105974.
Yang, T. hong, Shi, W. hao, Wang, P. tao, Liu, H. lei, Yu, Q. lei, Li, Y., 2015. Numerical simulation on slope stability analysis considering anisotropic properties of layered fractured rocks: a case study. Arab. J. Geosci. 8 (8), 5413–5421. https://doi.org/10.1007/s12517-014-1609-2.